

All Biodisintegratable Hydrogel Biohybrid Neural Interfaces with Synergistic Performances of Microelectrode Array Technologies, Tissue Scaffolding, and Cell Therapy

Wan-Lou Lei, Chih-Wei Peng, Shao-Chu Chiu, Huai-En Lu, Chun-Wei Wu, Tzu-Ya Cheng, and Wei-Chen Huang*

Biohybrid neural interfaces (BHNIs) are a new class of neuromodulating devices that integrate **neural microelectrode arrays (MEAs)** and **cell transplantation to improve treatment of nerve injuries** and disorders. However, current BHNI devices are made from **abiotic materials** that are usually **bio-passive, non-biodisintegratable, or rigid, which restricts encapsulated cell activity and host nerve reconstruction** and frequently leads to local tissue **inflammation**. Herein, the first MEA composed of all **disintegratable hydrogel tissue scaffold materials** with synergistic performances of **tissue conformal adhesiveness, MEA technologies, tissue scaffolding and stem cell therapy** on a time scale appropriate for nerve tissue repair is proposed. In particular, the MEA conductive tracks are made from **extracellular matrix (ECM)-based double-cross-linked dual-electrically conductive hydrogel (ECH)** systems with robust tissue-mimicking chemical/physical properties, electrical conductivity, and an **affinity for neural progenitor stem cells**. Meanwhile, the MEA hydrogel substrate prepared from **transglutaminase-incorporated gelatin/silk precursors** simultaneously promotes gelation and interfacial adhesion between all MEA stacks, leading to rapid and **scalable device integration**. When the full hydrogel MEA is subjected to various **mechanical stimuli and moisture**, it is structurally stable with a **low impedance ($4 \pm 3 \text{ k}\Omega$)** comparable to a recently reported benchmark. With **seamless lamination around peripheral nerve fibers**, the device **permits** successive neural **signal monitoring** for wound condition evaluation, while demonstrating synergistic effects of **spatiotemporally controlled electrical stimulation and cell transplantation** to accelerate restoration of **motor function**. This BHNI is completely degraded by **1 month** thus **eliminating** the need for surgical **retrieval** to stably remain, interact, and further fuse with host tissues, successfully exhibiting compatible integration of biology and an implanted electrical system.

1. Introduction

Implanted neural interfaces for neural prostheses have been successfully applied to treat neurological diseases and injuries.^[1] Lately, biologically inspired neural interfaces, called biohybrid neural interfaces (BHNIs), were declared the next-generation neural interfaces for improved device stability and functions.^[2] BHNIs that integrate neural electrodes and cell transplantation can permit cell-level electrical neuromodulation and neural signal recording to enhance nerve reinnervation, while encapsulated cells can evolve into a living mediated layer to reduce foreign tissue responses, providing active connections with various tissue structures, and even replacing injured tissues. Currently reported BHNIs are designed through cell decoration or a cell-laden polymeric coating on micromachined microelectrode arrays (MEAs) composed of metal tracks and rigid/flexible substrate materials such as silicon,^[3] polyimides,^[4] parylene C,^[5] or **polydimethylsiloxane (PDMS)**.^[6] Over a short period of implantation, the diminished cell reactivity results in exposure of the rigid device shank that further imposes mechanical damage to host tissues and hinders nerve reconnections. Because of the incompatibility between biology and electrical systems in BHNI devices, there are very few related reports.

W.-L. Lei, T.-Y. Cheng, W.-C. Huang
Institute of Biomedical Engineering
National Yang Ming Chiao Tung University
1001 University Rd., Hsinchu 30010, Taiwan

C.-W. Peng, C.-W. Wu
School of Biomedical Engineering, College of Biomedical Engineering
Taipei Medical University
250 Wu-Hsing Street, Taipei 11031, Taiwan

S.-C. Chiu
School of Biomedical Engineering
Taipei Medical University
250 Wu-Hsing Street, Taipei 11031, Taiwan

 The ORCID identification number(s) for the author(s) of this article can be found under <https://doi.org/10.1002/adfm.202307365>

DOI: 10.1002/adfm.202307365

In the field of nerve tissue engineering research, one of the efficient strategies for promoting nerve repair is to engineer tissue scaffolds with certain capabilities, including structural and mechanical properties imitating those of nerves, bioactivity to promote cell ingrowth, and degradability at an appropriate time after tissue reconstruction.^[7] Hydrogels with nerve tissue-mimicking viscoelasticity have been highly employed as nerve tissue scaffolds to support cell adhesion and encapsulation.^[8] Introduction of hydrogel coatings on BHNI highlights the higher viability of transplanted cells and better integration of devices and host tissues.^[9] Most recently, hydrogel electronics hold considerable promise in the revolution of implantable neural prosthetics by directly serving as MEA substrates.^[10] Applying hydrogel substrates to support microelectronic structures permits seamless and mechanically compliant contacts of the MEAs with curvilinear nerve tissues, in turn minimizing foreign tissue responses and leading to a high quality of neural signal transduction.^[11] However, most of the reported hydrogel substrate materials, such as polyvinyl alcohol (PVA),^[12] polyethylene glycol (PEG),^[13] silk fibrin,^[14] and alginate,^[15] are not biologically active and thus do not promote cell adhesion or growth. Moreover, in many cases the MEA passivation layer and conductive circuits remain stiff and non-disintegratable, and thus risks of chronic infections cannot be avoided.^[16] Effective implementation of BHNI relies on integrating tissue engineering materials into all MEA components, whereas these biologically permissive materials are electrically insulative and incompatible with most conventional device manufacturing processes.

Extracellular matrix (ECM) is a naturally occurring network entity surrounding and supporting cells in the body. Gelatin is one of the commonly used ECM-derived proteins that is recognized as an ideal bioactive site to enhance neuronal outgrowth in synthesized nerve tissue scaffolds.^[17] The employment of gelatin scaffolds to enhance engraftment of neural stem cells in vivo is a promising strategy to improve therapeutic nerve regeneration.^[18] Technically, gelatin can overcome the bottleneck of hydrogel fabrication by flexible crosslinking approaches, including temperature-dependent physical gelation, chemical crosslinking,^[19] photo-cross-linking,^[20] and enzyme cross-linking,^[21] to accommodate various microenvironments. In addition, many efforts have recently been made to endow gelatin with conductivity through combining gelatin

methacryloyl (GelMA) with conductive nanomaterials such as silver (Ag), carbon nanotubes (CNTs), graphene, or poly(3,4-ethylenedioxythiophene) (PEDOT): poly (styrene sulfonic acid) (PSS) for forming gelatin-based electroconductive hydrogels (ECHs).^[22] Accordingly, herein, electrically conductive hydrogels (ECHs) combined with PEDOT and GO was developed to permit nerve tissue compliant mechanical and structural properties, biocompatibility, and high electrical /biological activity. With both electroactivity and bioactivity, ECM-inspired ECHs can especially emulate the cell-habitable electrophysiological microenvironment of native nerve tissues, in which the supply of electrical stimulation guarantees more-efficient tissue rehabilitation.^[27] The precise control and versatility of gelatin and its derivatives provide the potential to greatly benefit BHNI technologies.

Therefore, by leveraging concepts derived from nerve tissue engineering and BHNI, we herein propose a new biodisintegratable, adhesive tissue scaffolding MEA (**Figure 1a,b**). The device substrate is made of an enzyme-crosslinked gelatin/silk (GS) hydrogel with adhesiveness and controllable degradability that benefit nerve tissue integration and neural progenitor cell (NPC) transplantation. MEA circuits composed of graphene oxide (GO)/PEDOT/gelatin-based ECHs were designed with a double-crosslinked architecture to confirm robust ionic/electroconductive properties. PEDOT stands out for its superior biocompatibility and electrical conductivity among various conductive polymers.^[23] GO is a highly promising 2D material applied in the neural interfaces due to the mechanical strength and rich oxygen-rich functional groups that can enhance neural adhesion, outgrowth, and neural signal transduction.^[24] It is well recognized that doping with negatively charged GO can stabilize the positively charged PEDOT due to charge balance, while the π - π interaction between PEDOT and GO enables the delocalization of π electrons, leading to the enhancement of the charge carrier mobility.^[25] Electrode materials composed of GO/PEDOT have been highly utilized in neural interfaces for the improved electrical and biological performances.^[26] We also introduce a new scalable enzyme-mediated transfer printing technology to achieve rapid and scalable device integration without using complex micromachine processing. The resultant all hydrogel MEAs were implanted at peripheral nerve injury sites to realize real-time electrical neuromodulation, nerve function monitoring, tissue scaffolding, and neural progenitor cell transplantation. This BHNI is expected to remain, interact, and further fuse with host tissues, successfully exhibiting synergistic effects of MEA functions and cell transplantation for advanced nerve injury care and accelerated nerve rehabilitation.

2. Results and Discussion

2.1. General Design of Hydrogel MEAs

Optical images of a cell-laden, adhesive, tissue scaffold-mimicking hydrogel MEA are shown in Figure 1c. The MEA consists of seven-channel microelectrodes with diameters of 150 and 300 μm which were fully fabricated with ECM-based ECHs with a thickness of 30 μm to ensure high electrical/electrochemical conductivity and complete conformational neural interfacing. Ultrathin and degradable PLA with a thickness of $\approx 1.5 \mu\text{m}$ was used as the passivation layer to insulate the MEA tracks. The MEA

H.-E. Lu
Institute of Biochemistry and Molecular Biology
National Yang Ming Chiao Tung University
75 Boai Street, Hsinchu 300, Taiwan

H.-E. Lu
Center for Regenerative Medicine and Cellular Therapy
National Yang Ming Chiao Tung University
75 Boai Street, Hsinchu 300, Taiwan

H.-E. Lu
Bioresource Collection and Research Center
Food Industry Research and Development Institute
331 Shih-Pin Road, Hsinchu 300193, Taiwan

W.-C. Huang
Department of Electrical and Computer Engineering
National Yang Ming Chiao Tung University
1001 University Rd., Hsinchu 30010, Taiwan
E-mail: weichenh@nycu.edu.tw

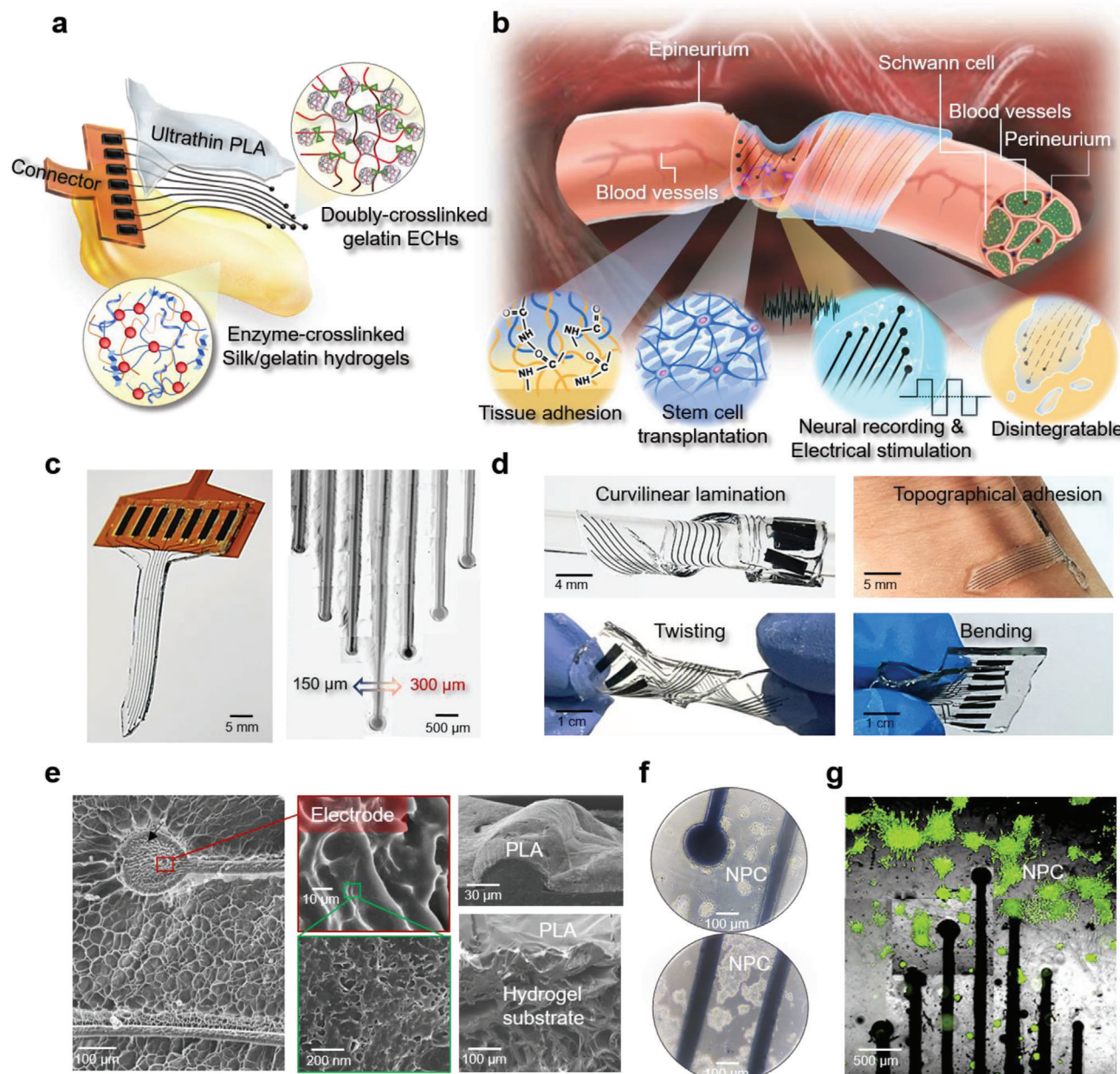


Figure 1. Extracellular matrix-inspired all hydrogel biohybrid neural interfaces. a) Schematic showing the proposed architecture and components of the microelectrode array (MEA) device. The MEA substrate is composed of bioactive, biodegradable, and adhesive silk/gelatin hydrogels. The MEA circuits are composed of bioactive and biodegradable gelatin-based electroconductive hydrogels (ECHs) with a double-crosslinked architecture, bonded with a flat printed circuit (FPC) board. With an ultrathin PLA passivation layer, the resultant device allows b) conformal contact with tissues, transient site-specific electrical stimulation, neural signal recording, nerve tissue scaffolding and cell therapy for improved treatment of peripheral nerve injury. c) Optical images of the hydrogel scaffold MEA containing seven channel microelectrodes with diameters (D_s) of 150 and 300 μm connected to the FPC. d) Demonstration of different mechanical deformation extents of the device, including curvilinear lamination, topographical adhesion, bending, and twisting. e) SEM images showing the high roughness and highly porous structure of the device. (f and g) Optical and fluorescence images, individually showing the neural stem cell adhesion and ingrowth on the MEA.

substrate, called GS-MTG, is an adhesive and stretchable hydrogel with an approximate thickness of 700 μm made from gelatin/silk (GS) cross-linked by microbial transglutaminases (MTGs). MTG is a Food and Drug Administration (FDA)-approved enzyme that encourages covalent

bonding interactions between gelatin and silk to achieve hydrogel gelation and promote adhesion. MTG also assists interfacial adhesion between MEA stacks, which in turn facilitates integration of all MEA components. Accordingly, the entire device demonstrated mechanical deformation,

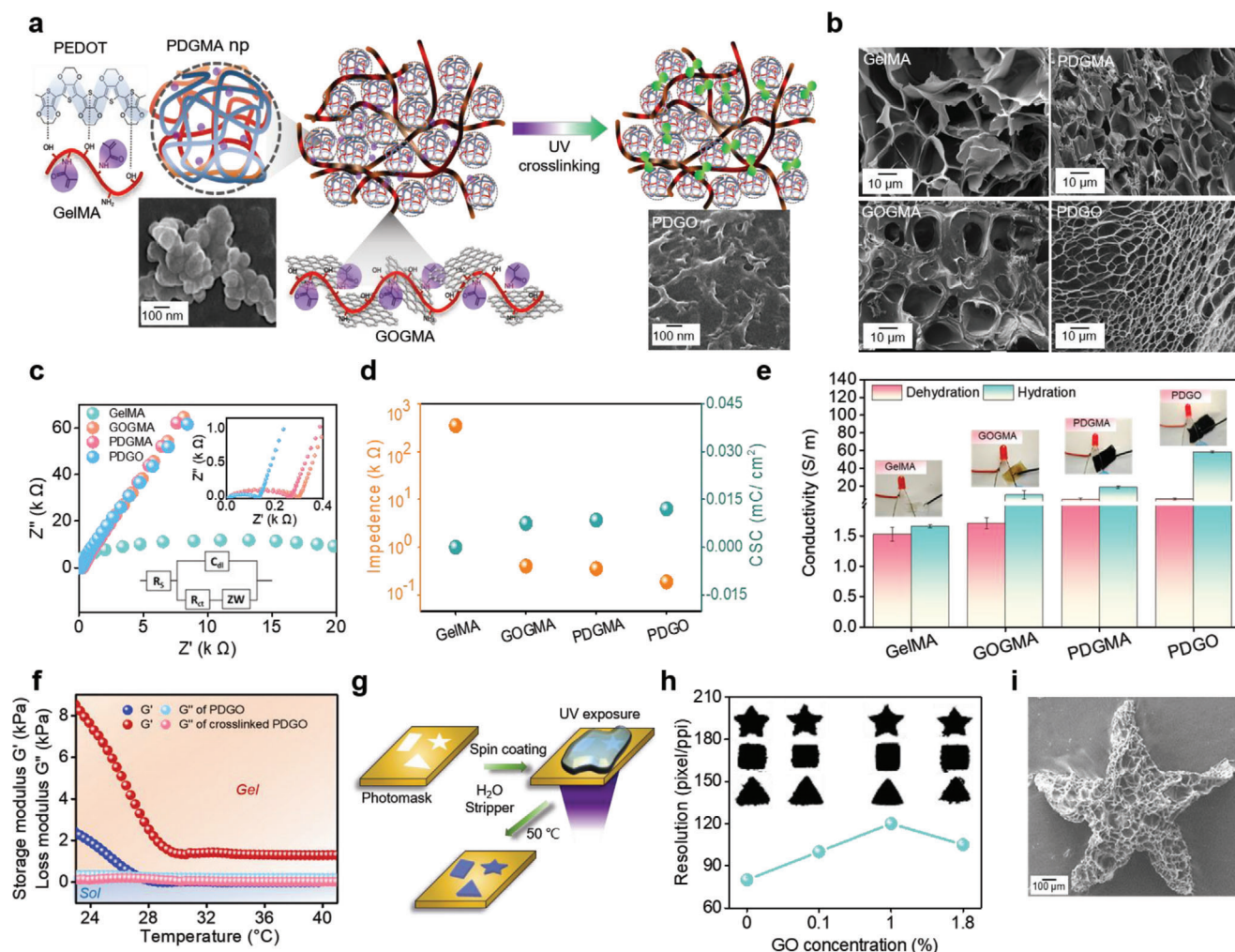


Figure 2. Synthesis and characteristics of PDGO electroconductive hydrogels (ECHs). a) Proposed mode for forming UV-curable PDGO ECHs from two-gel systems including GelMA-doped PEDOT (PDGMA) as sparsely soft nanogels and GelMA-modified graphene oxide (GO) (GOGMA) as a brittle skeleton. b) SEM images showing the porous microstructure of various hydrogels. c) Nyquist plots showing impedance spectra of various hydrogels and the corresponding equivalent circuit. d) The charge storage capacity (CSC) and impedance modulus at 1 kHz of different hydrogels (based on the area of a 1 × 1 cm coating on indium tin oxide (ITO)). e) Conductivity measurements of different hydrogels in hydrated and dehydrated states. Embedded images show the connected bulbs with different degrees of brightness. f) Temperature-dependent rheological behaviors of the PDGO before and after UV cross-linking. Viscosity was measured at increasing temperatures from 20 to 40 °C. g) Schematic illustration showing the fabrication process of PDGO micropatterns. h) PDGO micropatterns with various geometries showing tunable spatial resolution dependent on differences in GO concentrations. i) An SEM image showing the micropatterned PDGO with a porous microstructure.

including curvilinear lamination, topographical adhesion, bending, and twisting (Figure 1d). The full device displays a 3D network structure with high roughness and high porosity that facilitates mass/charge transfer and also enhances neural stem cell adhesion and ingrowth (Figure 1e,f).

2.2. Synthesis and Characteristics of ECM-based ECHs

ECHs permitting both ionic and electrical conductivity are regarded as ideal neural interface materials.^[28] In this study, the ultraviolet (UV)-cured ECHs had a double-crosslinked architecture composed of two gel systems, i.e., **GelMA-doped PEDOT (PDGMA)** as sparsely soft nanogels and **GelMA-modified GO**

(GOGMA) as a **brittle skeleton** (Figure 2a).^[29] Compared to dispersing PEDOT nanoparticles in GelMA with two individual phase systems, in-situ doping of the negatively charged GelMA in EDOT monomers under oxidation and polymerization yielded a single-phase water-dissolvable PDGMA nanogel with a relatively lower percolation threshold in moisture (with a greater than 5-fold decrease in resistance compared to PEDOT when being hydrated, i.e., 10.1 vs. $3.2 \times 10^6 \Omega$)^[28,30] (Figure S1, Supporting Information). To further enhance the conductivity, the as-formed positively charged PDGMA nanogels were crosslinked with negatively charged graphene oxide (GO)-conjugated GelMA (GOGMA) (Figure S2, Supporting Information), forming the final hierarchical structural PDGO. SEM images in Figure 2a,b show that PDGO demonstrated a microporous structure with

a higher pore density and higher degree of interconnections compared to those of GelMA, PDGMA, and GOGMA, revealing faster transport of charge carriers within the gel. In addition, the π - π interaction between PEDOT and GO may cause the delocalization of π electrons, leading to the increment of the charge carrier mobility of PDGO.^[8] Such bonding interaction can be explained by the mechanical properties shown in Figure S3 and Table S1 (Supporting Information), where PDGO displayed higher tensile strength, toughness, and ductility as compared with those of PDGMA and GOGMA.

The charge mobility of PDGO ECHs was evaluated by impedance measurements. Nyquist plots in Figure 2c are explained by a proposed equivalent circuit model of a constant-phase element, i.e., a Randles circuit that represents double-layer capacitor behavior of rough electrodes.^[31] PDGO showed the smallest semicircle representing the smallest solution and charge-transfer resistances (R_s and R_{ct} , respectively) compared to the other hydrogels, which was attributed to the higher roughness of PDGO (Figure S4, Supporting Information) associated with larger electroactive sites. Meanwhile, PDGO also showed the lowest impedance value of 0.136 k Ω at 1 kHz in the corresponding Bode plot (Figure 2d; Figures S5, Supporting Information). Moreover, all of the CV curves in Figure S5 (Supporting Information) show equirectangular shapes representing a non-faradic charging/discharging process for these hydrogels. By integrating the enclosed areas of the CV profiles, PDGO had the highest CSC value (0.012 mC cm⁻²) compared to the other hydrogels (Figure 2d). A similar result was observed in the measured electrical conductivity in Figure 2e, where PDGO presented the highest conductivity ($\sigma_{dry} = 5.46$ S m⁻¹, $\sigma_{wet} = 58.5$ S m⁻¹). These results are also consistent with those obtained from SEM images in Figure 2b, indicating that PDGO with a higher density of porosity and interconnection favored electrical percolation.

2.3. Micropatterning of ECHs

In Figure 2f, PDGO presents a gelatin-derived reversible thermoresponsive sol-to-gel phase-transition behavior.^[32] Figure 2f displays storage modulus G' and loss modulus G'' simultaneously in the temperature-dependent rheologic measurement. The intersection between G' and G'' of the pristine PDGO at 27 °C represents that as the temperature achieves the value the bulk hydrogel transforms to random coils that could be dissolved in water. However, for the crosslinked PDGO, there is no intersection occurring between G' and G'' , revealing that the hydrogel is thermally stable without dissolution. Accordingly, PDGO coated onto a photomask could be directly micropatterned through UV exposure followed by stripping with hot water (Figure 2g). PDGO could be fabricated into variable geometries with tunable spatial resolutions dependent on the GO concentration (Figure 2h). Increasing the GO concentration in PDGO resulted in an increment in the hydrogel cross-linking density that increased the spatial resolution of the as-formed patterns. However, excessive incorporation of GO roughened the pattern profile. PDGO with a 1% GO concentration showed the highest pattern resolution with a line width down to 30 μ m. The SEM image in Figure 2i shows that the micropatterned PDGO in a delicate starlike shape preserved a 3D microporous network structure.

2.4. Fabrication of Hydrogel MEAs

Fabrication of hydrogel MEAs does not need complex micro-electronic manufacturing workflows or an expensive facility, but it follows four processes operated on one and the same photomask (Figure 3a): 1) screen-assisted solvent casting of PLA suspensions as a passivation layer; 2) UV-curing of the ECHs as MEA electrodes and tracks; 3) formation of a hydrogel substrate through a sol-gel transition; and 4) enhanced interfacial adhesion to integrate the hydrogel substrate with the other MEA stacks. In an inverted architecture of MEAs, a PLA film with thickness of < 2 μ m is required to present high transparency that allows photo-curing of the PDGO tracks (Figure 3b). A cell-laden and adhesive hydrogel substrate composed of MTG-crosslinked GS hydrogels (GS-MTG) was created for several reasons. MTG catalyzes crosslinking of gelatin and silk by producing amide bonds between the glutamine and lysine groups, yielding gels with elasticity and robust interfacial adhesion to MEA stacks^[33] (Figure 3c). MTG-crosslinked gelatin hydrogels are well-known tissue scaffolds with controllable degradation rates for enhancing stem cell adhesion, proliferation and differentiation.^[34] Finally, GS-MTG can produce covalent bonds with tissue proteins, serving as cost-effective, non-toxic, and resorbable soft-tissue adhesives.^[35]

MTG simultaneously mediates the sol-gel transition and adhesion enhancement, which was determined by the MTG concentration and reaction time. Figure 3d shows the kinetics of GS-MTG hydrogel formation dependent on the MTG concentration in precursor solutions. Precursors containing more than 0.4% MTG produced hydrogels that could be handled and exhibited an elastic modulus (G') of > 4 kPa, which approximated that of nerve tissues. The catalysis also imparted interfacial adhesion between hydrogels and the MEA insulator (PLA) and conductor (PDGO). Adhesion was measured via recording force-distance curves between PLA- and PDGO-coated probes and hydrogel substrates. Representative force-distance curves are shown in Figure S6 (Supporting Information), where hydrogels permitted robust adhesion to both PLA and PDGO. The effective tensile work of adhesion $W_{ten,eff}$ achieved the highest value within 90 min of catalysis (Figure 3e), afterwards a decay of $W_{ten,eff}$ revealed that crosslinking within GS may have dissipated interfacial adhesion. Interestingly, MTG enabled a higher degree of catalysis between gelatin and silk than that between gelatin itself, which contributed to the highest $W_{ten,eff}$ compared to those of gelatin and gelatin-MTG (Figure 3f). It is worth noting that adhesion was also imposed on the interface between hydrogels and hydrophobic PLA, which may be attributed to enhanced intermolecular hydrogen bond interactions.^[36] Adhesion measurement was also applied on nerve and muscle tissues. The result shown in Figure S6 (Supporting Information) demonstrates similar results obtained between hydrogel-device surfaces, where GS-MTG hydrogels permit the highest adhesion intensity on tissue surfaces than gelatin and gelatin-MTG. Accordingly, catalysis permitted simultaneous hydrogel gelation and interfacial adhesion with the underlying MEA, enabling direct integration of all of the MEA components without applying a sacrificial layer. This transfer printing method is feasible in a large area of 8 \times 8 cm², contributing to the production of batch hydrogel devices in one step (Figure 3g).

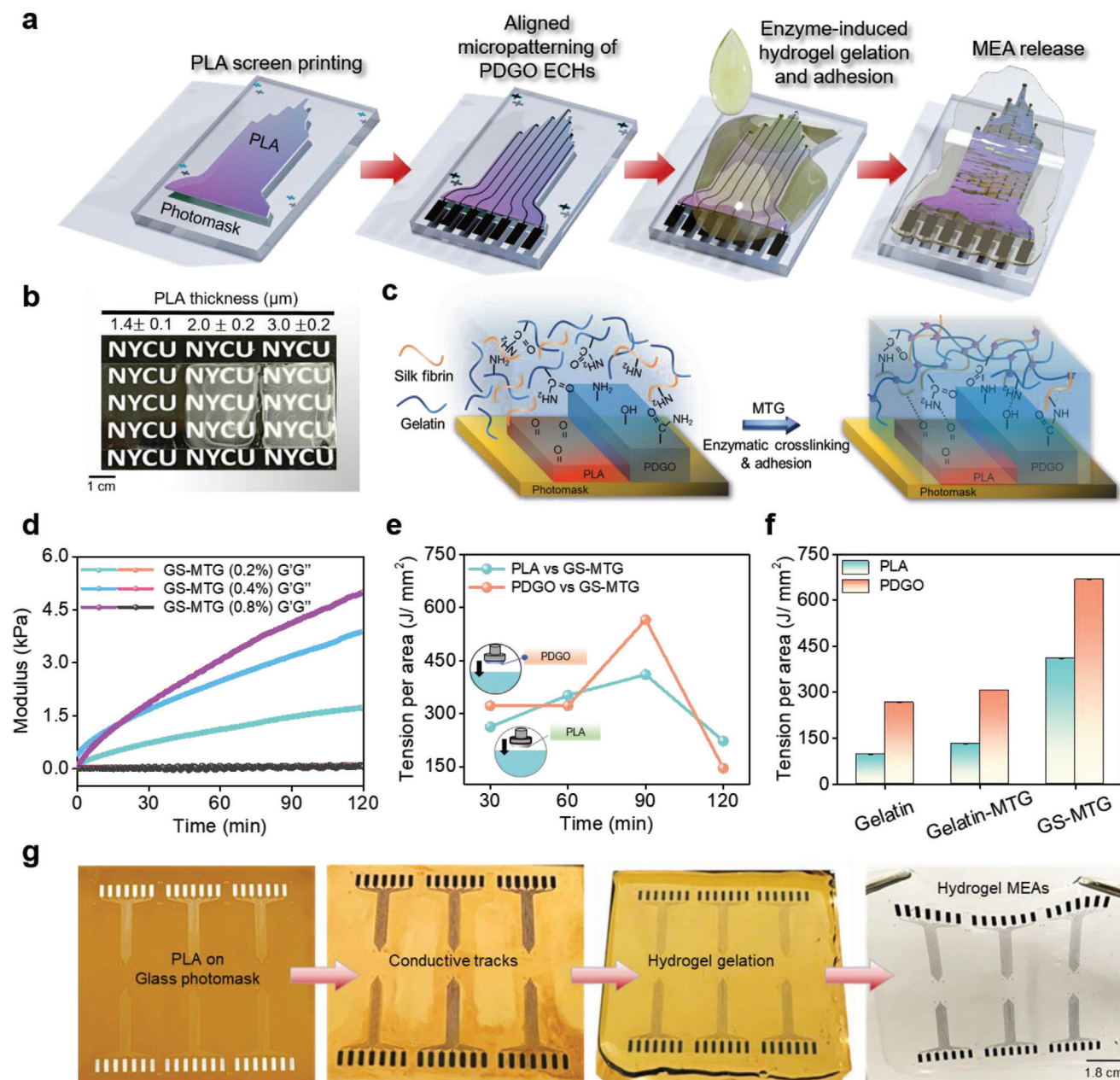


Figure 3. Microfabrication of whole hydrogel microelectrode arrays (MEAs). a) Process flow of the fabrication of the conformable all-hydrogel MEA. Steps included (i) screen-printing of PLA suspensions as a passivation layer; ii) alignment and micropatterning of PDGO electroconductive hydrogels (ECHs) as MEA tracks; iii) sol-gel transition of the gelatin/silk (GS)-microbial transglutaminase (MTG) hydrogel precursor; and iv) transfer-printing of MEA stacks on the hydrogel substrate inspired by enhanced interfacial adhesion. b) Thickness-dependent light transmittance of PLA. c) Schematic drawing demonstrating that the MTG in GS simultaneously mediates the sol-gel transition of the hydrogel precursors and adhesion enhancement between hydrogels and the bottom substrate. d) The viscoelasticity (G' and G'') versus time of GS-MTGs with different MTG concentrations in precursor compositions. e) Effective work of adhesion $W_{ten,eff}$ versus time monitored at the PLA/GS-MTG and PDGO/GS-MTG interfaces. f) Effective work of adhesion $W_{ten,eff}$ recorded at $t = 90$ min after gelation of gelatin, gelatin-MTGs, and GS-MTGs on PLA and PDGO surfaces. g) Naked views showing the all MEA components were integrated into the final devices. The process proves that batch production of devices was obtained.

2.5. Structural and Electrical Stability of Hydrogel MEAs

For hydrogel electronic devices, surface instability is frequently observed from interfaces between hydrogels and rigid thin film, where hydrogel swelling often induces compression stresses that cause the layered structure to deform, delaminate, or fracture.^[37]

To evaluate the structural stability of hydrogel MEAs, interface stresses of three different bilayer systems, including hydrogel/metal (Au), hydrogel/PLA, and hydrogel/ECH stacks of various thicknesses, were simulated by a finite element analysis (FEA) (Figure S7, Supporting Information). Hydrogel swelling produced relatively larger interfacial compression stresses to

metal (Au) thin films compared to hydrogel/PLA and hydrogel/ECHs bilayer systems with almost no interfacial stresses. Our previous study reported that hydrogel-based MEAs composed of Pt and parylene C required a thick SU-8 support layer (with thickness, t , of $\approx 26 \mu\text{m}$) to absorb interfacial stresses.^[38] In this study, both MEA tracks and substrate were composed of hydrogels, and thus the mechanical match could stabilize the entire device structure without deformation in moisture (Figure S7, Supporting Information).

The electrochemical performance of each MEA channel was assessed to confirm the site-specific signal transduction of the hydrogel MEA. Electrodes with diameters, D , of 150 and 300 μm showed stable CV profiles at a wide voltage window of -0.4 – 0.9 V in PBS (Figure S8, Supporting Information). The calculated charge storage capacity (CSC) derived from five devices reached $24.3 \mu\text{C cm}^{-2}$, which is comparable to those recorded from numerous pure conductive polymers or carbon microelectrodes^[39] (Figure S8, Supporting Information). The impedance modulus at 1 kHz exhibited magnitudes ranging 1.7 to 2.3 $\text{k}\Omega$, which were among the lowest ones of reported neural MEAs (1.0–2.5 $\text{k}\Omega \text{ mm}^2$). CV lifetime tests were performed to investigate the electrochemical stability of the device. After 100 CV cycles, hydrogel MEAs still preserved CSC values (at 1 kHz) of $30 \pm 12 \mu\text{C cm}^{-2}$ and impedance values of $2.1 \pm 0.9 \text{ k}\Omega$ (Figure S8, Supporting Information). To evaluate the mechanical stability, impedance at 1 kHz under different mechanical deformation extents was measured (Figure 4a–c). The electrochemical performance of smaller electrodes is influenced by mechanical stimuli more profoundly than that of larger ones. For electrodes with a diameter, D , of 150 μm , the impedance showed an increment of up to 5.2 $\text{k}\Omega$ in response to the uniaxial tensile strain that ranged 0%–33%. The twisted device preserved the impedance of 4.8 $\text{k}\Omega$ when the torsional angle reached 720° . The device with folding at angles of up to 135° resulted in impedance increases of up to 17.7 $\text{k}\Omega$. The above results indicated that the hydrogel MEA undergoing various mechanical deformation extents still exhibited the electrochemical performance that met the benchmark of neural recording systems.^[10b,40] The hydrogel MEAs were disintegrable to alleviate the requirement of invasive and costly retrieval procedures. The device undergoing “hydrolysis” over time was demonstrated in *in vitro* degradation experiments in PBS (Figure 4d). Although the device lost more than 45% of its original weight by day 7 in PBS, the hydrogel degradation following a bulk erosion mechanism enabled preservation of the device construction for electrochemical measurements.^[41] After 28 days of *in vitro* degradation, the device still exhibited a CSC of $1.99 \mu\text{C cm}^{-2}$ and impedance of $1.6 \pm 0.8 \text{ k}\Omega$ compared to original values.

2.6. Cell Activity and Differentiation on Hydrogel MEAs

The hydrogel MEA provides a bioactive microenvironment to enhance iPSC-derived NPC adhesion, growth, and differentiation. Cell viability was assessed on each MEA component including GS-MTG, PLA, and PDGO, as demonstrated in Figure S9a,b (Supporting Information). After 72 h of culture, cells that adhered to the control (culture dish), GS-MTG, and PDGO exhibited virtually no cell death, while the number of surviving cells (stained

in green) on PLA was relatively lower. This can be attributed to the hydrophobicity of PLA that inhibited adhesive protein adsorption for NPC attachment.^[42] The poor cell-PLA interaction can localize cell distributions on electrode sites. Additionally, PDGO exhibited significantly high cell viability in this group, indicating that the presence of GO in PDGO had minimal toxic effects on NPCs. To confirm that NPCs were undergoing motor neuron differentiation, the HB9 marker, specific to motor neurons, was utilized. HB9 expression indicates activation of the motor neuron-specific promoter and serves as a reliable indicator of motor neuron differentiation in NPCs. Fluorescent images and statistical results shown in Figure 4e,f and Figure S9 (Supporting Information) indicate that HB9 was highly expressed in cells on GS-MTG and PDGO, which could be attributed to the robust cell-material affinity that led to activation of motor neuron-specific genes and initiation of motor neuron differentiation pathways.^[43] Thus, the hydrogel provided a supportive microenvironment that facilitated the commitment of NPCs towards motor neurons.

2.7. Site-Specific Peripheral Nerve Recording and Stimulation of Hydrogel MEAs

Performing high-resolution nerve recording and stimulation by implanted tissue reconstruction scaffolds is highly productive for treating nerve injuries and disorders. A schematic of peripheral neural signal recording and electrical stimulation is shown in Figure 5a. Pads of the hydrogel scaffold MEAs were connected to a customized flexible flat circuit board (FCB) using silver paste and encased in PDMS (Figure 5b). After being placed on the sciatic nerve of a rat, the hydrogel MEA exhibited the measured impedance response of ≈ 1 – $2 \text{ k}\Omega$ at a frequency range of 100 Hz to 10 kHz (Figure 5c). These values matched those recorded *in vitro* as shown in Figure 4. For neural signal recording, the skin of the left hind paw was mechanically stimulated by a compression force. The evoked compound nerve action potentials (CNAPs) recorded using bipolar electrodes constructed by two selected microelectrodes with different microelectrode spacings are demonstrated in Figure 5d. It was found that the mechanical stimuli could be verified by the hydrogel MEA, and meanwhile, the distance between two microelectrodes ($D1 = 1 \text{ mm}$, $D2 = 2 \text{ mm}$, and $D3 = 3 \text{ mm}$) greatly influenced the amplitude and noise of the CNAPs. Increasing the electrode distance resulted in an increment in the measurement depth, leading to a higher CNAP amplitude and less interference.^[44] When the electrode spacing was 3 mm ($D1$), the optimal CNAP recording was obtained with the highest amplitude potential. This indicated that the spatial arrangement of the microelectrodes has an impact on the recorded electrical signals. These CNAP signals were further processed by fast Fourier transformation (FFT). Accumulation of the frequency power showed that all electrode distance conditions ($D1$, $D2$, and $D3$) could correctly measure a stimulated compression force event compared to the unstimulated control condition (Figure 5e). Moreover, in the $D1$ condition, the CNAP recording exhibited the widest-range frequency spectrum of up to 1000 Hz compared to $D2$ and $D3$ conditions (Figure 5f). This suggests that the specific electrode spacing used in the study had a favorable impact on the recorded CNAP

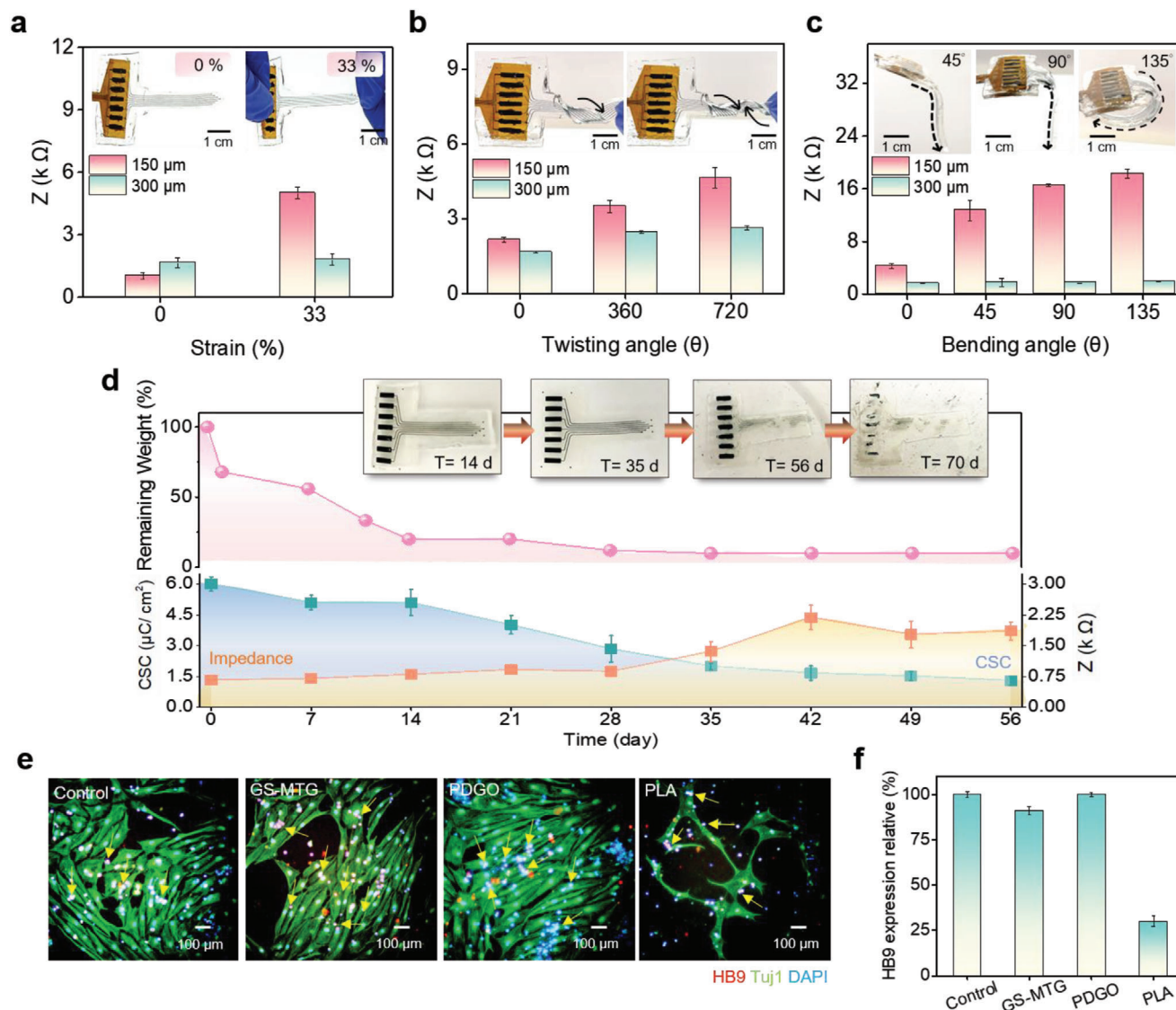


Figure 4. Structural and electrical stability of the hydrogel microelectrode arrays (MEAs). a–c) Impedance recorded at 1 kHz for devices subjected to stretching, twisting, and bending to show device stability when mechanically deformed. d) Naked views and corresponding remaining weights of hydrogel MEAs degraded in PBS at 37 °C. Real-time recording of impedance values at 1 kHz, and the charge storage capacity (CSC) was also demonstrated. e) Fluorescence images of neuron progenitor cell (NPC) distribution on different MEA components after 14 days of differentiation. Cells were immunohistochemically stained with an early-stage motor neuron marker, HB9, and neuron marker, Tuj1 f) Statistical intensity analysis of early-stage motor neuron marker (HB9) expression.

characteristics. Subsequently, the amplitude of electromyographic (EMG) responses in the calf muscle evoked by electrical stimulation (ES) was used as readouts of peripheral nerve excitability. Under ES application with various current amplitudes (1, 3, and 5 mA), higher electrical activity was obtained by ES with larger currents, indicating that a stronger ES elicited a larger muscle force (Figure 5g). Meanwhile, the larger electrode spacing also resulted in more-significant EMG performance (Figure 5h). These results revealed that hydrogel scaffold MEAs could provide conformal contact with nerve tissues to allow both site-specific signal recording and excitability of motor function of the sciatic nerve.

2.8. Hydrogel MEAs with Combined Treatments of MEA Technologies and Tissue Engineering on Peripheral Nerve Injury

Hydrogel MEAs with functions including tissue scaffolding (MEA group), stem cell transplantation (MEA/NPC group), electrical monitoring and stimulation (MEA/ES group), and combined multiple functions (MEA/NPC/ES group) were applied to manage peripheral nerve injury. Here, an axotomy injury with epineurial damage was created for NPC transplantation (Figure 6a). Wound recovery could be extensively monitored by neural signal recording using the hydrogel MEA (Figure 6a,b). The CNAP amplitude showed a significant drop

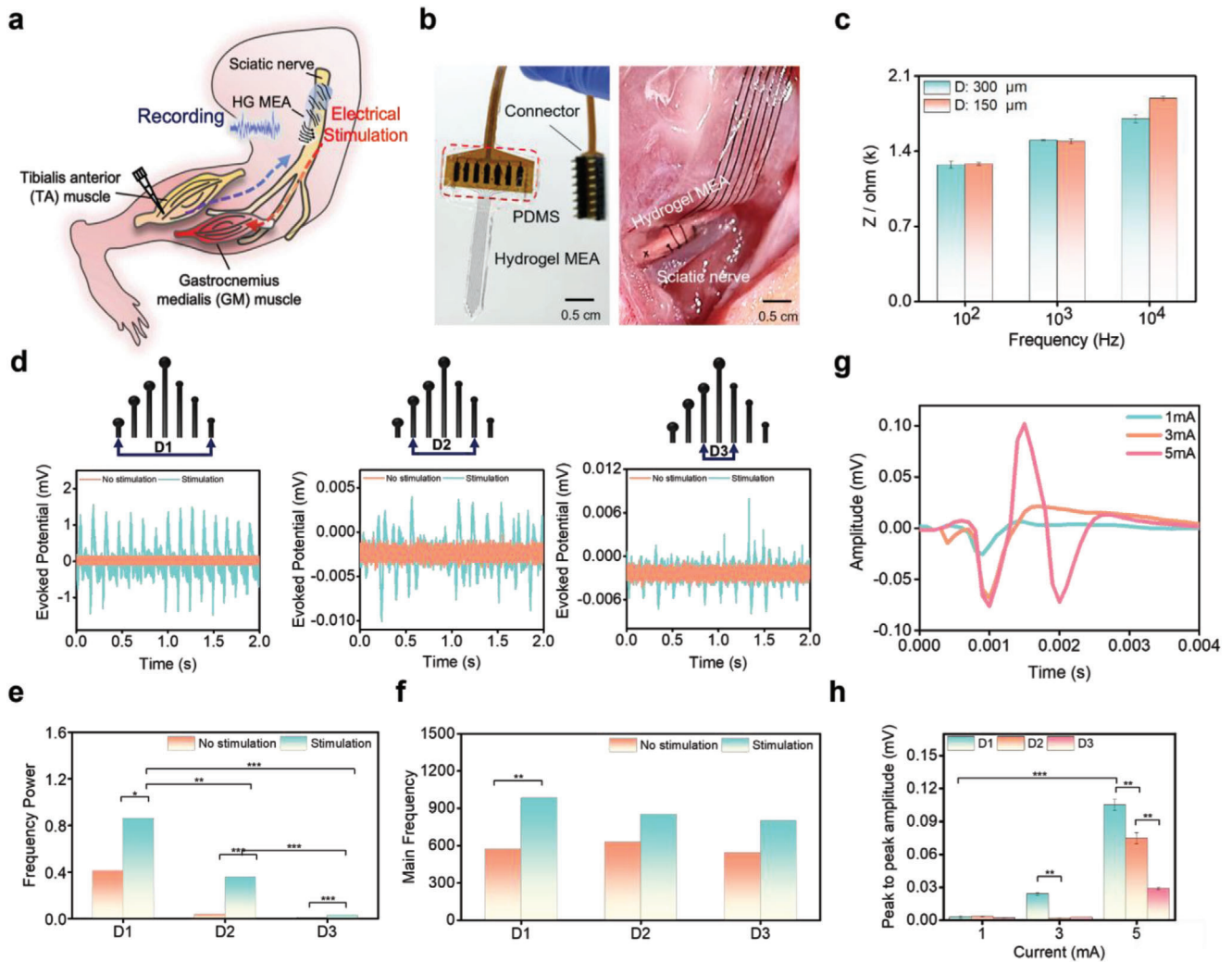


Figure 5. In vivo site-specific peripheral neural signal recording and stimulation. a and b) Schematic and optical images, respectively, of the hydrogel microelectrode arrays (MEAs) placed on a sciatic nerve. c) In vivo recorded impedance values at frequencies of 102, 103, and 104 Hz. d) Sensory neural signal recording using bipolar electrodes with different microelectrode spacings. e and f) Statistical frequency power and main frequency of sciatic nerve signals as a function of microelectrode spacings. h) Motor evoked potentials (MEPs) obtained at the gastrocnemius muscle (GM) when electrical stimulation (ES) with different current intensities (1, 3, and 5 mA) was applied through a hydrogel MEA with bipolar electrodes at a spacing of 3 mm. f) Statistical MEP amplitude as a function of the applied current intensity.

after lesion creation on day 1 for all groups, indicating functional loss of the damaged nerves. Although the device mostly degraded and failed to provide signal information after 14 days of implantation, obvious differences in peak amplitudes among different groups were found by day 7. We calculated the CNAP ratio based on the signal recorded before injury and at time, t , to define the degree of restoration (Figure 6b). Combined treatment (MEA/NPC/ES group) showed the highest degree of restoration of 60% on day 7 compared to those of other groups, revealing the robust effect on nerve reinnervation.

Subsequently, locomotor recovery was observed by recording walking tracks and sciatic function index (SFI) scores at indicated time points.^[45] Referring to footprint patterns in Figure S10 (Supporting Information), different degrees of toe spread were observed in each group at 7, 14, and 28 days. According to the quantified SFI values by day 14, all treatments led to more-

improved toe spread resulting from wound healing compared to the control group, while the MEA/NPC/ES group exhibited the most pronounced effect of function recovery, which corresponded to the results of neural signal monitoring (Figure S10b, Supporting Information). Meanwhile, according to the observation on the post-injury grip strength analysis, all the treatments including MEA, MEA/NPC, MEA/ES and MEA/ES/NPC contributed to improved effects on the motor recovery, while the MEA/ES group exhibited higher healing efficiency than the MEA/NPC group and the MEA/NPC/ES group exhibited the highest performance. (Figure S10c, Supporting Information). The effects of cell transplantation and ES on wound healing were further investigated by immunostaining of tissue sections.

In particular, expression of the microtubule-associated protein (MAP2), a neuron-specific cytoskeletal protein,^[46] can display

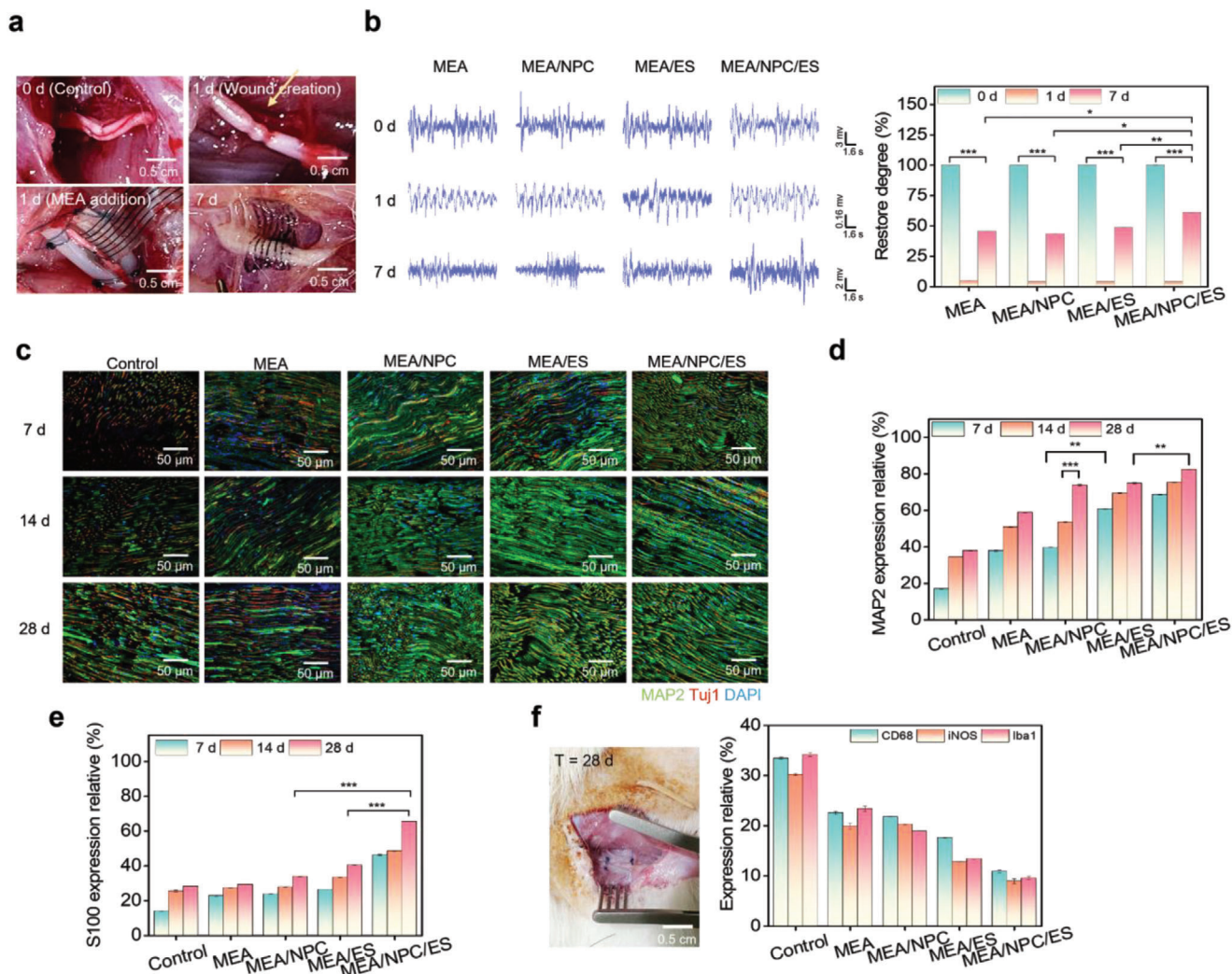


Figure 6. Effects on sciatic nerve wound healing based on various treatments including electrical modulation, tissue scaffolding, and cell therapy provided by hydrogel microelectrode arrays (MEAs). a) Images showing the sciatic nerve that was exposed and crushed, followed by being wrapped with the hydrogel MEAs. b) Real-time nerve signal recording at the injury site under various treatments. Time-dependent degree of restoration (RD) calculated based on the change in the neural potential amplitude at the injury site. (c) Confocal images showing immunohistochemical staining of a neuron-specific cytoskeletal protein marker (MAP2), and neuron marker (Tuj1). Results of the statistical intensity analysis are shown in d). e and f) Intensity analysis of S100 β (top) and CD68 expressions (bottom), respectively. A significant difference was indicated by * $p < 0.05$ and ** $p < 0.01$. Statistical analysis included a one-way ANOVA with the post-hoc Tukey HSD test (mean \pm SEM).

the degree of regenerated neurons that may come from either transplanted NPCs or local tissues.^[47] In the early stage of wound healing (by day 7) the MEA/ES group showed more-significant MAP2 expression than did the MEA/NPC group; however, at a later stage (by day 28), MAP2 expression of the MEA/NPC group demonstrated a dramatic increase, even achieving a comparable level to that of the MEA/ES group (Figure 6c,d). These results can be attributed to the application of ES that permitted a prompt effect on neuromodulation, while NPCs provided by the hydrogel MEA only demonstrated improved neuron function after differentiation.^[48] Moreover, the MEA/NPC/ES group showed higher MAP2 expression compared to the MEA/ES group in the entire healing duration, confirming that ES can further promote NPC differentiation into functional neurons.^[49] Successive

neuron axon growth of injured nerves was further evaluated by observing the expression of a myelin-specific protein (S100 β).^[50] Results of a quantitative analysis in Figure 6e clearly showed that S100 β expression of the MEA/NPC/ES group was higher than those of other groups, which successfully demonstrates the synergistic effects of ES and cell transplantation on accelerated restoration of motor function. Concerning the negative impact of degraded device debris on tissues, acute immune responses were investigated by day 28 post-injury, the expression levels of pertinent inflammatory markers (CD68, iNOS, Iba1) (Figure 6f) in various groups exhibited a pattern consistent with that of MAP2 and S100 β , suggesting that following disintegration, these devices did not induce an acute macrophage response but rather fostered a conducive environment for accelerated remyelination.

3. Conclusions

In this study, a fully biodisintegratable ECM-based BHNI was developed to improve nerve injury management. The BHNI reported here is the first MEA composed of all biodisintegratable hydrogel scaffold materials that enabled tissue-device adhesiveness, MEA technology, nerve tissue support, and cell therapy with no need for surgical removal to prevent infections associated with foreign tissue responses. Double-crosslinked dual GelMA-based ECH systems established MEA conductive tracks with robust electrical/ionic conductivity, cell affinity, and tissue-mimicking structural and mechanical properties. Meanwhile, the gelatin/silk MEA hydrogel substrate prepared from transglutaminase-incorporated precursors simultaneously promoted hydrogel gelation and interfacial adhesion between all MEA stacks to achieve rapid and cost-effective device integration at a scalable level without using expensive facilities or complex parameter controls. With the mechanical compatibility of all the hydrogel MEA stacks, the device demonstrated structural stability in response to various mechanical stimuli and moisture. The device allowed seamless wrapping around peripheral nerve fibers to permit successive neural signal monitoring for evaluation of wound conditions, while demonstrating synergistic effects of implanted scaffold, ES, and cell transplantation on accelerated restoration of motor function. This study successfully presents the efficacy of transient bioelectronic medicine for treating host tissues based on the conceptual combination of neural interfaces and tissue engineering. The degradability of the device can be tailored to a large degree by the hydrogel material composition to ensure more-chronic treatment of severe nerve injuries such as neurotmesis, and spinal cord or brain traumatic injuries. The overall fusion of the biology and electrical systems also invokes potential applications in treating other electroactive soft tissues such as skeleton and cardiac muscles, or other electrically modulable soft organs.

4. Experimental Section

Materials: Graphite powder (average mesh size of 325 and a purity of 99.8%) was purchased from Alfa Aesar (J65261 – Alfa Aesar, MA, USA). Silkworm cocoons were purchased from the Agricultural Research and Extension Station (Gongguan Township, Miaoli County, Taiwan). Microbial transglutaminase (MTG) was purchased from Bioman Scientific Ltd. (New Taipei, Taiwan). Methacrylic anhydride (MA), sodium carbonate (Na_2CO_3), phosphorus pentoxide (P_2O_5), potassium persulfate ($\text{K}_2\text{S}_2\text{O}_8$), hydrogen peroxide (H_2O_2) solution, lithium bromide (LiBr), iron III acetylacetonate, chloroform, paraformaldehyde, Triton X-100, dihydrochloride (DAPI), 3,4-ethylenedioxythiophene (EDOT), Geltrex, iron (II) chloride tetrahydrate (99.0%), and a polylactic acid (PLA, MW $\approx 60\,000$) dialysis cassette (3.5 K MWCO, 12 mL) were purchased from Sigma–Aldrich (St. Louis, MO, USA). Nerve growth factor (NGF), fetal bovine serum (FBS), horse serum (HS), Dulbecco's modified Eagle medium/nutrient mixture F-12 Ham (DMEM/F12), bovine serum albumin (BSA), penicillin-streptomycin, trypsin-EDTA, β -tubulin III (Tuj1), S100, and anti-rabbit Hilyte 488 (1/100, 61056-H488, AnaSpec, Fremont, CA, USA), and anti-mouse Alexa Fluor 405 (1/100, A-31553, Molecular Probes Invitrogen, Carlsbad, CA, USA) were purchased from ThermoFisher Scientific (Sensititre; Thermo Fisher Scientific, Cleveland, OH, USA). iNOS, and Iba1(1/100, #IRAP5017, iReal Biotechnology, Hsinchu, Taiwan). CytoSelectTM was purchased from Cell Biolabs (San Diego, CA, USA). Sprague-Dawley (SD) rats were purchased from BioLASCO Taiwan (Nangang Dist., Taipei, Taiwan).

Preparation and Characteristics of PDGO Conductors: GelMA was synthesized based on Lee's method.^[51] Briefly, gelatin was completely dissolved in phosphate-buffered saline (PBS, pH 7.4), followed by adding MA at pH 7. The mixed solution was dialyzed to remove unreacted MA and other byproducts. Finally, the ultimate solution was freeze-dried for storage. A 10% GelMA water solution was prepared in 9.4 mL of deionized water at 50 °C. $\text{FeCl}_3 \cdot 6\text{H}_2\text{O}$ and EDOT (Fe^{3+} : EDOT = 3:1 mol mol⁻¹) were added to the GelMA solution followed by stirring overnight at 50 °C to carry out oxidative polymerization. The product of a dark-blue color was washed with water/ethanol (1:9) three times and dried at 55 °C overnight. The final product, called PDGMA, was dissolved in water at a concentration of 1.68 wt.%, followed by casting into a dry film. To investigate bonding interactions, a Fourier transform infrared spectroscopic (FTIR) analysis using a 100 FTIR spectrometer was performed with 50 scans at a resolution of 4 cm⁻¹ (PerkinElmer, Waltham, MA, USA). GOGMA was prepared from graphite using modified Hammer's method.^[52] Briefly, 1 g of native graphite flakes was preoxidized with the addition of 1 g of P_2O_5 , 1 g of $\text{K}_2\text{S}_2\text{O}_8$, and 3 mL of H_2SO_4 , and then incubated at 80 °C for 6 h. After washing with deionized water followed by filtering, the preoxidized graphite was dried overnight at 60 °C in an oven. Subsequently, the preoxidized graphite powder was further oxidized in 23 mL of H_2SO_4 with the slow addition of KMnO_4 followed by stirring at 35 °C for 2 h. After 2 h, the reaction was terminated by adding 140 mL of distilled water. Subsequently, a hydrogen peroxide solution (H_2O_2 , 30% in water) was added until the color of the mixture turned from black to yellow. Finally, the mixture was centrifuged at 11 000 rpm for 30 min to remove excess H_2O_2 . To the resultant GO solution was added GelMA (GO: GelMA = 1:10 g g⁻¹) to form a 1% GOGMA solution. The final PDGO was prepared with 1.68% PDGMA and 1% GOGMA in 1 ml of double-distilled (dd) H_2O and stirring at 50 °C.

Zeta potential (ZP) measurements were carried out using a Malvern Zetasizer Nano ZS instrument (Malvern Panalytical Ltd, UK). Triplicate samples were measured three times each at 25 °C. The particle size distribution of PDGO was examined by dynamic light scattering (DLS, DelsaTM Nano C, Beckman, USA) on a diluted PDGO solution (0.1 wt.%). The morphologies of GelMA, PDGMA, GOGMA, and PDGO hydrogels were observed using scanning electron microscopy (SEM, JEOL-JSM6700, Tokyo, Japan) with an accelerating voltage of 10 kV. Stress–strain measurements were performed by uniaxial testing on the as-prepared hydrogels using MTS Tytron 250 (MTS Systems Corp., Minnesota, MN, USA). Each dry sample was cut into a rectangular shape of 3 cm in length and 1 cm in width. The applied load was set in a window range of 0 to 50 N at a working rate of 0.1 mm⁻¹ s. The PDGO gelation dynamics were indirectly measured using a rheometer (TA Instruments, New Castle, DE, USA) in a parallel plate geometry. Freshly prepared precursor solutions were applied to the center of the plate with a nominal gap distance of 800 μm . Storage (G') and loss (G'') moduli were measured by a linear time sweep along with increasing temperature (strain amplitude, γ , of 1% and angular frequency, ω , of 1 Hz for 2 h). Sheet resistances of GelMA, PDGMA, POGMA, and PDGO were measured using a four-point probe (Jandel RM3000, Leighton Buzzard, UK). The resistivity of the sample was calculated as described by Equation (1). The conductivity of the sample was calculated as described by Equation (2)

$$\text{Resistivity} = \text{Sheet resistance} \times \text{Thickness} \quad (1)$$

$$\text{Conductivity} = 1/\text{Resistivity} \quad (2)$$

Electrochemical properties were investigated using the electrochemical 600E Potentiostat/Galvanostat instrument (CH Instruments, Austin, TX, USA), with a standard three-electrode system (an indium tin oxide (ITO) glass substrate coated with hydrogel samples in an area of $1 \times 1 \text{ cm}$ as a working electrode, a platinum wire as a counter electrode, and an Ag/AgCl reference electrode in 0.1 M PBS). Impedance responses were assessed by applying amplitude sinusoids of 100 mV across a frequency range of 1 Hz to 1 MHz. The mean impedance magnitude was presented in a Bode plot and a Nyquist plot obtained by the average of three scans for each sample. For cyclic voltammetric (CV) measurements, the scan rate was 50 mV s⁻¹, and the applied potential window was set to -0.4 to 1.0 V with 50 scan

cycles. The surface roughness of the hydrogels was investigated using a 3D optical microscope (PA53MET 3D, Motic, Vancouver, Canada) and analyzed using Motic Images Advanced 3.2 software. To fabricate micropatterned PDGO, the precursors were spin-coated onto a photomask with various patterns. Following UV exposure and a hot water (50 °C) wash, the resultant patterned PDGO was obtained. FITC-conjugated PDGO was also prepared for observation by confocal laser scanning microscopy (CLSM, D-eclipse, Nikon, Tokyo, Japan). Then, color contrasts of CLSM images were analyzed by ImageJ software to calculate the pixel per inch (PPI) used to define the pattern resolution.

Preparation and Characteristics of GS-MTG and PLA: Silk fibroin was purified based on a protocol described by Danielle et al.^[53] Briefly, an aqueous silk fibroin solution was prepared by degumming silkworm cocoons in a 0.02 M Na₂CO₃ solution, followed by gentle washing with distilled water. The products were dried overnight and then dissolved in 9.3 M LiBr at 60 °C for 4 h. The silk protein solution was then purified by dialysis (Slide-A-Lyzer Dialysis Cassettes, 3.5 K MWCO, 66 333, Thermo Scientific, Rockford, IL, USA) against distilled water for 48 h to obtain a 6%–8% w/v silk solution. GS-MTG hydrogels were prepared in a water solution according to the weight ratio of gelatin: silk: MTG of 1.1:0.4:0.75. For gelation dynamic exploration, freshly prepared GS-MTG precursor solutions containing different MTG concentration (0.2%, 0.4%, and 0.8%) were applied to the center of the plate with a nominal gap distance of 800 μm. The storage (G') and loss (G'') moduli were measured by a linear time sweep (strain amplitude, γ, of 1% and as angular frequency, ω, of 1 Hz for 2 h). Interfacial adhesion was measured between freshly prepared GS-MTG or gelatin-MTG hydrogels and the PLA- or PDGO-coated indenter. Hydrogels with cylindrical form factors (D × h = 20 × 2 mm) were mounted on the platform. Indenters with flat cylindrical glass windows (D = 5 mm; Edmund Optics, Barrington, NJ, USA) were attached to a vertical motorized stage for indentation, with the measured loads at a 1 kHz sampling rate, the indenter with a constant preload force of 50 ± 5 mN for the contact with the hydrogels for 5 min, followed by retraction at a constant speed of 1 mm⁻¹ s, and then force-distance curves were recorded. PLA thin films with different thicknesses were prepared by a solvent-evaporated coating using 0.1 mL of a PLA chloroform solution with concentrations of 1%, 2%, and 3% on a glass substrate. The thickness of the PLA films was measured using a profilometer (Dektak XT, Bruker, Billerica, MA, USA). Three replicates of this measurement were necessary to obtain an acceptable standard deviation (SD).

Fabrication of Hydrogel MEAs by Transfer Printing: A schematic drawing of the fabrication process flow is shown in Figure 3a, where a patterned PLA thin film was deposited through a stencil mask aligned with an underlying photomask. The homogeneously distributed PDGO solution prepared by ultrasound treatment was spin-coated onto the photomask to obtain a thickness of 30–32 μm, followed by UV exposure for complete crosslinking. After immersion in water at 50 °C to remove unreacted residues, the MEA tracks were obtained. To proceed with transfer printing, the freshly prepared GS-MTG precursor solution was dropped onto the as-formed PLA-PDGO stacks. After 1.5 h of gelation, the hydrogel was retrieved, and the PLA-insulated MEAs were transfer printed onto GS-MTG. The transfer-printing process turns all the MEA stacks upside down, which further allows for the exposure the electrode channel sites.

Simulated Stress Evolution of Swollen Devices: A finite element analysis (FEA) was performed using COMSOL Multiphysics. Interfacial stress of MEAs was simulated as the ECH hydrogel (represented by PDGO), PLA, and metal layer were laminated to hydrogel substrates (represented by GS-MTG). The device was simulated using guided-end conditions with prescribed displacement of 0 in the y- and z-directions at either end of the device. One corner of the device was fixed to satisfy the force balance in the system. A solid mechanics model with a hygroscopic swelling module was used to simulate the swelling of the hydrogel. The swelling ratio of GS-MTG and PDGO was calculated by Equation (3). Three samples of each hydrogel type were tested.

$$\text{Swelling ratio} = \frac{W_t - W_0}{W_0} \times 100\% \quad (3)$$

where W_0 and W_t are the weights of the hydrogel at initial time and time t , respectively.

Electrochemical Performance of Hydrogel MEAs: To investigate the electrical performance of hydrogel MEAs, bond pads were connected to a customized fabricated flexible flat circuit board (BioLASCO Taiwan Co., Ltd, Taipei, Taiwan) using silver paste and were encased in PDMS silicone (Dow Corning, Auburn, MI, USA) for protection. The electrochemical properties of the device were determined by electrochemical impedance spectroscopy (EIS) and CV. The setup and measurement parameters were referred to those described in 4.2. In addition, the electrode performance and stability were analyzed by CV lifetime tests to determine cyclic redox reactions. In this study, all samples were evaluated by a lifetime test with 100 CV cycles. The degradation test followed that described by Zustiak et al.^[54] GelMA: PDGO hydrogels were completely immersed in deionized water at room temperature to test the water uptake capacity. Samples were weighed at different time intervals after swelling.

The in vitro biodegradation of hydrogels was studied by incubating them in a PBS solution and then monitoring their weight-loss following different incubation times. Samples were immersed in PBS and weighed every 7 days and after ethanol treatment for 5 min. After removal from PBS, water drops were gently wiped from the surface. The mass loss of the sample was calculated as described in Equation (4):

$$\text{Mass loss} = \frac{m_t - m_0}{m_0} \times 100\% \quad (4)$$

where m_t is the mass at the degradation time point and m_0 is the original mass of the sample.

Stem Cell Growth and Differentiation on Hydrogel MEAs: Cell culture: In this study, iPSC-derived neuron progenitor cells (NPCs; iNPC03), the best candidate for modeling neuronal degenerative disorders,^[55] were used for the in vitro study. A flow cytometric analysis of Oct4, nestin, Sox2, and Pax6 expressions of NPCs indicated the complete differentiation of MSCs into NPCs (Figure S13, Supporting Information). First, cells were seeded on a sample with Neurobasal medium (Gibco, Thermo Fisher Scientific, Waltham, MA, USA) supplemented with 1% B-27 Supplement (Gibco, Thermo Fisher Scientific, Waltham, MA, USA). iNPC03 cells were incubated at 37 °C in a 5% CO₂ moist atmosphere, and sub-culture by treatment with trypsin-EDTA (Gibco, Thermo Fisher Scientific, Waltham, MA, USA) in a 37 °C incubator for 3 min, and then centrifuged at 1500 rpm for 5 min. The iNPC03 passage process was conducted every 4 days each week. Cells were cultured in CultureOne Supplement (Gibco, Thermo Fisher Scientific, Waltham, MA, USA) to facilitate their differentiation into mature neuron cells.

In vitro cytotoxicity: Cytotoxicity was explored using a CytoSelect™ cell viability and cytotoxicity assay (Cell Biolabs, San Diego, CA, USA). Live-dead reagents included calcium-AM for staining living cells (green) and ethidium homodimer (EthD)-1 for staining dead cells (red). Cells were seeded onto the electrodes with 1 × 1 cm area at 2.5 × 10⁵ cells well⁻¹. After 24 h of cell culture, the diluted live/dead reagents in PBS were directly added to the cell culture media at a ratio of reagent to culture media of 1:1, followed by gentle mixing. After incubation in the dark for 30 min, five representative fields of view were selected per well under a fluorescent microscope. Numbers of live (green) and dead (red) cells were counted using the multi-wavelength cell scoring module of MetaMorph software. All data are reported as the mean ± standard deviation (SD) of tests performed in triplicate. Statistical analysis was carried out by a one-way analysis of variance (ANOVA) followed by Student's *t*-test to determine statistical significance ($p < 0.05$).

Cell immunofluorescence (IF) staining: For cell differentiation, cells were seeded at 2.5 × 10⁴ cells well⁻¹ at 1 cm in area. After being cultured with CultureOne Supplement in Neurobasal medium for 7 to 14 days, neuronal differentiation of iNPC03 cells was determined by IF staining by the following procedures. First, cells were fixed with 4% paraformaldehyde (Sigma-Aldrich, St. Louis, MO, USA) for 15 min at room temperature, then washed with PBS three times. Next, cells were permeabilized with 0.25% Triton X-100 (J.T Baker, center valley, PA, USA) for 15 min at room temperature. After being washed with PBS three times, cells were nonspecifically blocked

by 2% (w/v) bovine serum albumin (BSA) for 60 min. Subsequently, cells were immersed in a 1:250 dilution of class III β -tubulin (Tuj1, GT11710, GeneTex, Louis, MO, USA), and HB9 / HLXB9 (GTX134781, GeneTex, Louis, MO, USA) in the dark for 1 h, then stained with a 1:250 dilution of Alexa Fluor 488 goat anti-mouse (Invitrogen, ref. A11001, Waltham, MA, USA) and DyLight594 goat anti-rabbit immunoglobulin G (IgG) antibody (GTX213110-05, GeneTex, Louis, MO, USA) for 1 h in the dark at room temperature. Afterwards, nuclei of cells were stained with a 1:1000 dilution of DAPI (Invitrogen; Thermo Fisher Scientific, Inc., Waltham, MA, USA) for 15 min in the dark at room temperature. Images were captured using a Nikon Eclipse TE2000-U microscope (Tokyo, Japan). ImageJ software was used to evaluate the percentage of differentiated cells on the electrodeposited substrates. Representative fields of view were selected based on an adequate cell density without a large bare region on the plate. Particularly, a field containing ≈ 40 cells using a 10 \times objective was selected for statistical analysis. The percentage of differentiated cells was obtained from the number of cells present within the microscope field of view. For each photo, three views were selected, and at least three photos of each sample were analyzed. Significance was defined as * $p < 0.05$, ** $p < 0.01$, and *** $p < 0.001$. In all cases, error bars represent the standard error of the mean (SEM).

NSC cell culture on hydrogel MEAs: iNPC03s cells were maintained in tissue culture plates in growth medium at 37 °C and 5% CO₂. Hydrogel MEAs were sterilized by incubation in 70% ethanol for 1 h, followed by washing with sterile PBS and exposure to UV light for 1 h. Cells were detached from plates with a 0.05% w/v trypsin/EDTA solution and seeded at a density of 5.0×10^4 cells cm⁻² at the devices. Then growth medium was replaced with differentiation medium, which was exchanged every 2 days.

Animal Preparation and Device Implantation: In vivo peripheral nerve signal recording and stimulation: All experimental procedures were approved by the Institutional Animal Care and Use Committee (IACUC) of the Taipei Medical University Laboratory Animal Center. Adult male Sprague-Dawley (SD) rats weighing 300–370 g was used for sciatic nerve recording. Rats were anesthetized with zoletil (50 mg k⁻¹ g; Vibac Laboratories, Carros, France). Throughout the experiment, rats were placed on a heating pad, and their breathing rate was monitored every 15 min. To prepare for the procedure, the hair on both sides of the femur was clipped, and the area was cleaned and sterilized using Betadine and 75% ethanol. Once the rats had reached a deep level of anesthesia, a skin incision was made, extending to the dorsal aspect of the paw to expose the right sciatic nerve. Retractors (17009-07, Fine Science Tools Inc., Foster City, CA, USA) were used to maintain visibility during the procedure. The sciatic nerve was carefully lighted and [placed/covered?] with a hydrogel MEA. In the in vivo experiment, the hydrogel MEAs were connected to FCB using silver paste, followed by encased in PDMS for stabilization, in addition, the MEAs/FCB interface is left outside the body to avoid water invasion. Ground and reference wires were placed on the right hind legs. Sciatic nerve signals were recorded using the BIOPAC MP36/Recording Controller (Biopac Systems Inc., Goleta, CA, USA) and BIOPAC MP36 amplifier at a sampling rate of 10 kHz. Different electrode spacings, namely D1 (3 mm), D2 (2 mm), and D3 (1 mm), were used for signal detection. The experimental protocol involved initial neural recordings during a baseline period with no stimuli. Subsequently, a force of 0.245 N was applied to the gastrocnemius muscle (GM) at 10 s intervals, followed by 10 s rest periods, to elicit sensory responses in the nerve. The collected data were processed by dividing them into 10 segments, each containing 2048 data points, for a fast Fourier transform (FFT) analysis. After FFT, a frequency range of 60 to 1225 Hz was selected as the main frequency of interest, and integration was applied using the BIOPAC controller (Biopac Systems Inc., Goleta, CA, USA) to minimize ambient noise and movement artifacts. Statistical significance was determined as follows: $p < 0.05$, $p < 0.005$, and $p < 0.001$. Error bars in all cases represent the standard error of the mean (SEM). For electrical stimulation, another needle was inserted into the GM for electromyographic (EMG) recording. The MEA was connected to an external stimulator (A-M Systems/Recording Controller and A-M Systems amplifier, Intan Technologies LLC., Los Angeles, CA, USA). Amplifier gain was set to 1000 with the output of the amplifiers bandpass-filtered at 300 Hz to 10 kHz. EMG record-

ings were conducted with the leg in a natural relaxed position to prevent any movement restrictions. Stimuli were delivered in the form of constant voltage pulses (10 Hz) with an intensity from 1 to 5 mA and every 1 s to gradually elicit nerve responses. Electrode distances used for stimulation were D1 (3 mm), D2 (2 mm) and D3 (1 mm). CAPs were continually recorded before and after stimulation, and responses were saved to data files.

In vivo neural signal recording and stimulation for sciatic nerve injury: Creation of peripheral nerve crush injury and in vivo implantation procedures were approved by the Institutional Animal Care and Use Committee (IACUC) of the Taipei Medical University Laboratory Animal Center and performed following guidelines for the care and use of animals. After exposure of the sciatic nerve by the surgery described above, the nerve was crushed at a point 5 mm distal to its origin using Adson-Brown tweezers for a duration of 5 min. Subsequently, the hydrogel MEA ($n = 3$ per group) was wrapped around the crushed sciatic nerve after removing the surrounding tissues. The device was fixed onto the sciatic nerve using a silicone tube, and the f connector was positioned in the neck area within the muscle and subcutaneous space. Muscle and skin incisions were separately sutured, and animals were allowed to recover while being regularly monitored during the study. At specific time points ($t = 0, 1, 7$, and 14, and 28 days), animals were euthanized using the anesthetic rompun (10 mg k⁻¹ g; Bayer, Leverkusen, Germany). Nerves were harvested and processed for a histological analysis. Electrophysiology was conducted post-transplantation to collect electrical signals from the sciatic nerves. Rats were anesthetized with 2% isoflurane in balanced oxygen under sterile and body-temperature warming conditions.

For electrical stimulation, animals in the stimulation group ($n = 3$) were connected to the A-M system via the connector. Biphasic pulses were delivered to the chosen stimulation channel at an average of 10 Hz and constant voltage pulses of 3 mA for cycles of 5 min on/5 min off at 80% of movement threshold, which activates neurons without causing large contractions. Stimulation was administered for 27 days, every 3 days, starting 3 days after injury.

Analysis of walking tracks: To evaluate sciatic nerve functional recovery of rats in each group, a walking track analysis was performed at 7, 14, and 28 days post-surgery. Rats were led to the entrance of a narrow channel (10 \times 10 \times 60 cm) and were guided to walk toward the exit to record the walking track. Three metrics were measured to calculate the sciatic function index (SFI), including paw length (PL, distance from the third toe to the heel), toe spread (TS, distance from the first to the fifth toes), and intermediary toe spread (IT, distance from the second to the fourth toes). The SFI was calculated using the following formula:

$$SFI = -38.3 \times \frac{EPL - NPL}{NPL} + 109.5 \times \frac{ETS - NTS}{NTS} + 13.3 \times \frac{EIT - NIT}{NIT} - 8.8 \quad (5)$$

where E is the experimental side and N is the normal side. An SFI equal to -100 indicates total impairment, whereas an SFI oscillating ≈ 0 is considered to reflect normal function.

Analysis of grip strength test: Animals were tested using a grip strength meter (303500-M/E, TSE Systems, Chesterfield, MO, USA), consisting of a grasping grip (6 cm wide) connected to a sensor module. During the test, the animal was fixed around the shoulders with the left hand, while the right hand held the lower body, and the legs grasped a grid connected to a force transducer with its hind legs and was then pulled by the tail with increasing force until the grip was eventually lost. The animal grasped the grip and was slowly and consistently pulled by the tail until it detached from the grip. The applied maximum force was measured during three repetitive trials and averaged.

Tissue section IF: Section IF followed that described by Hsu et al.^[56] At 7, 14, and 28 days post-surgery, harvested nerves were removed and fixed in 4% paraformaldehyde at pH 7.4 for 5 h at 4 °C. Following fixation, nerves were then washed in PBS three times for 10 min each time. After fixation, a nerve was sectioned and embedded in optimum

cutting temperature compound. Horizontal cryostat sections were sliced and then stained for an immunohistochemical analysis. To ensure better antibody penetration for nerve-crushed samples, the epineurium was removed in these preparations after washing in PBS. Then, sections were stained overnight at 4 °C with the primary antibody solutions. The obtained slides were stained as follow: 1) β -III tubulin (1:100) for regenerated axons; 2) S100 β (1:100) for Schwann cells; 3) MAP2 (1:100) (the predominant cytoskeletal regulator within neuronal dendrites); 4) CD68 (1:100) (a protein highly expressed by cells in the monocyte lineage); 5) iNOS (1:100) (a potent signaling molecule that can be produced by various cell types, including macrophages themselves); 6) and Iba1 (1:100) (a calcium-binding protein, is exclusively expressed in macrophages and microglia). The secondary antibody was stained for 2 h using Alexa 488 and then washed three times with PBS. Next, the section was stained with DAPI (1:200) for 30 min and then washed three times with PBS. The morphology of all the stained sections was observed using a Multiphoton Confocal Microscope System (MCMS) (TCS-SP5-X AOBs, Leica, Mannheim, Germany). The intensity and alignment of regenerating axons were analyzed by Image ProPlus and ImageJ software, respectively. * $p < 0.05$, ** $p < 0.005$, and *** $p < 0.001$ indicated significant differences as analyzed by a one-way ANOVA with post-hoc Tukey honest significant difference (HSD) test, and results are presented as the mean \pm standard error of the mean (SEM).

Supporting Information

Supporting Information is available from the Wiley Online Library or from the author.

Acknowledgements

W.-L.L. and C.-W.P. are contributed equally to this work. The authors thank for the research grants of MOST 110-2636-E-009-012; NSTC 111-2636-E-A49-007 and MOST 108-2636-E-009-013 from National Science and Technology Council in Taiwan. The authors would like to thank National Yang Ming Chiao Tung Nano Facility Center and Taiwan Semiconductor Research Institute for support and maintenance of the fabrication equipment, and iReal Biotechnology for resource support in immunostaining experiments.

Conflict of Interest

The authors declare no conflict of interest.

Data Availability Statement

Research data are not shared.

Keywords

cell therapy, hydrogel electronics, microelectrode arrays, neural interface, peripheral nerve injury, transient electronics

Received: June 28, 2023
Revised: September 12, 2023
Published online:

[1] a) A. Gummadavelli, H. P. Zaveri, D. D. Spencer, J. L. Gerrard, *Front. Neurosci.* **2018**, *12*, 474; b) D. Valeriani, F. Santoro, M. Ienca, *Front. Neurobot* **2022**, *16*, 953968.

- [2] a) A. E. Rochford, A. Carnicer-Lombarte, V. F. Curto, G. G. Malliaras, D. G. Barone, *Adv. Mater.* **2020**, *32*, 1903182; b) D. O. Adewole, M. D. Serruya, J. A. Wolf, D. K. Cullen, *Front. Neurosci.* **2019**, *13*, 269.
- [3] a) K. D. Wise, D. J. Anderson, J. F. Hetke, D. R. Kipke, K. Najafi, *Proceedings of the IEEE* **2004**, *92*, 76; b) K. D. Wise, *IEEE Engin. Medic. Bio. Magaz.* **2005**, *24*, 22; c) S. M. E. Merriam, O. Srivannavit, M. N. Gulari, K. D. Wise, *J. Microelectromech. Syst.* **2011**, *20*, 594.
- [4] a) D. A. Soscia, D. Lam, A. C. Tooker, H. A. Enright, M. Triplett, P. Karande, S. K. G. Peters, A. P. Sales, E. K. Wheeler, N. O. Fischer, *Lab Chip* **2020**, *20*, 901; b) P. J. Rousche, D. S. Pellinen, D. P. Pivin, J. C. Williams, R. J. Vetter, D. R. Kipke, *IEEE Trans. Biomed. Eng.* **2001**, *48*, 361.
- [5] a) Y. Morikawa, S. Yamagiwa, H. Sawahata, R. Numano, K. Koida, M. Ishida, T. Kawano, *Adv. Healthcare Mater.* **2018**, *7*, 1701100; b) R. Cornuéjols, A. Albon, S. Joshi, J. A. Taylor, M. Baca, S. Drakopoulou, T. R. Barkat, C. Bernard, S. Rezaei-Mazinani, *ACS Appl. Mater. Interfaces* **2023**, *15*, 22854.
- [6] a) E. K. Purcell, J. P. Seymour, S. Yandamuri, D. R. Kipke, *J. Neural Eng.* **2009**, *6*, 026005; b) J.-W. Yang, C.-Y. Chen, Z.-Y. Yu, J. H. Y. Chung, X. Liu, C.-Y. Wu, G.-Y. Chen, *Materials Today Bio.* **2022**, *14*, 100253; c) N. Adly, S. Weidlich, S. Seyock, F. Brings, A. Yakushenko, A. Offenhäusser, B. Wolfrum, *npj Flexible Elect.* **2018**, *2*, 15.
- [7] a) Z. Liu, X. Wan, Z. L. Wang, L. Li, *Adv. Mater.* **2021**, *33*, 2007429; b) B. Newland, H. Newland, F. Lorenzi, D. Eigel, P. B. Welzel, D. Fischer, W. Wang, U. Freudenberg, A. Rosser, C. Werner, *ACS Chem. Neurosci.* **2021**, *12*, 1178; c) D. Angius, H. Wang, R. J. Spinner, Y. Gutierrez-Cotto, M. J. Yaszemski, A. J. Windebank, *Biomaterials* **2012**, *33*, 8034.
- [8] J. Cai, H. Zhang, Y. Hu, Z. Huang, Y. Wang, Y. Xia, X. Chen, J. Guo, H. Cheng, L. Xia, W. Lu, C. Zhang, J. Xie, H. Wang, R. Chai, *J. Nanobiotechnol.* **2022**, *20*, 460.
- [9] V. A. Kornev, E. A. Grebenik, A. B. Solovieva, R. I. Dmitriev, P. S. Timashev, *Comput. Struct. Biotechnol. J* **2018**, *16*, 488.
- [10] a) M. Bansal, Y. Vyas, Z. Aqrave, B. Raos, E. Cheah, J. Montgomery, Z. Wu, D. Svirskis, *ACS Biomater. Sci. Eng.* **2022**, *8*, 3933; b) Y. Liu, J. Li, S. Song, J. Kang, Y. Tsao, S. Chen, V. Mottini, K. Mcconnell, W. Xu, Y.-Q. Zheng, J. B.-H. Tok, P. M. George, Z. Bao, *Nat. Biotechnol.* **2020**, *38*, 1031; c) C. M. Tringides, N. Vachicouras, I. De Lázaro, H. Wang, A. Trouillet, B. R. Seo, A. Elosegui-Artola, F. Fallegger, Y. Shin, C. Casiraghi, K. Kostarelos, S. P. Lacour, D. J. Mooney, *Nat. Nanotechnol.* **2021**, *16*, 1019.
- [11] A. F. Renz, A. M. Reichmuth, F. Stauffer, G. Thompson-Steckel, J. Vörös, *J. Neural Eng.* **2018**, *15*, 061001.
- [12] a) D. V. S. K. Gunapu, Y. B. Prasad, V. S. Mudigunda, P. Yasam, A. K. Rengan, R. Korla, S. R. K. Vanjari, *Int. J. Biol. Macromol.* **2021**, *176*, 498; b) Y. Lu, Y. Li, J. Pan, P. Wei, N. Liu, B. Wu, J. Cheng, C. Lu, L. Wang, *Biomaterials* **2012**, *33*, 378.
- [13] a) I. K. Han, K. I. Song, S. M. Jung, Y. Jo, J. Kwon, T. Chung, S. Yoo, J. Jang, Y. T. Kim, D. S. Hwang, *Adv. Mater.* **2022**, *35*, 2203431; b) Z. J. Du, C. L. Kolarcik, T. D. Y. Kozai, S. D. Luebben, S. A. Sapp, X. S. Zheng, J. A. Nabity, X. T. Cui, *Acta Biomater.* **2017**, *53*, 46; c) J. H. Park, S. Hwang, J. Kwak, *Langmuir* **2011**, *27*, 8548.
- [14] a) W.-C. Huang, C.-C. Lin, T.-W. Chiu, S.-Y. Chen, *ACS Appl. Mater. Interfaces* **2022**, *14*, 46188; b) N. Adly, T. F. Teshima, H. Hassani, G. A. Boustani, L. J. K. Weiß, G. Cheng, J. Alexander, B. Wolfrum, *Adv. Healthcare Mater.* **2023**, *12*, 2202869; c) Y. Zhou, C. Gu, J. Liang, B. Zhang, H. Yang, Z. Zhou, M. Li, L. Sun, T. H. Tao, X. Wei, *Microsyst. Nanoeng.* **2022**, *8*, 118.
- [15] a) S. Karimi, Z. Bagher, N. Najmoddin, S. Simorgh, M. Pezeshki-Modaress, *Int. J. Biol. Macromol.* **2021**, *167*, 796; b) L. Ferlauto, A. N. D'angelo, P. Vagni, M. J. I. Airaghi Leccardi, F. M. Mor, E. A. Cuttaz, M. O. Heuschkel, L. Stoppini, D. Ghezzi, *Front. Neurosci.* **2018**, *12*, 648.
- [16] a) Y. Liu, J. Liu, S. Chen, T. Lei, Y. Kim, S. Niu, H. Wang, X. Wang, A. M. Foudeh, J. B.-H. Tok, Z. Bao, *Nat. Biomed. Eng.* **2019**, *3*, 58; b) H.

- Yamamoto, L. Grob, T. Sumi, K. Oiwa, A. Hirano-Iwata, B. Wolfrum, *Adv. Biosyst.* **2019**, *3*, 1900130.
- [17] B. Jin, Y. Yu, X. Chen, Y. Yang, Y. Xiong, Y. J. Im, Y. Zhao, J. Xiao, *Bioactive Mater.* **2023**, *21*, 511.
- [18] a) H. Ke, H. Yang, Y. Zhao, T. Li, D. Xin, C. Gai, Z. Jiang, Z. Wang, *Adv. Sci.* **2023**, *10*, 2204528; b) M. R. Arkenberg, K. Koehler, C.-C. Lin, *Biomacromolecules* **2022**, *23*, 4141.
- [19] Y. Ding, R. Ma, G. Liu, X. Li, K. Xu, P. Liu, K. Cai, *ACS Appl. Mater. Interfaces* **2023**, *15*, 45539.
- [20] P. Weng, K. Liu, M. Yuan, G.-Q. Huang, K. Wu, X. Yang, H. Dai, W. Lu, D. Li, *Small* **2023**, *19*, 2301012.
- [21] D. Wang, S. Maharjan, X. Kuang, Z. Wang, L. S. Mille, M. Tao, P. Yu, X. Cao, L. Lian, L. Lv, J. J. He, G. Tang, H. Yuk, C. K. Ozaki, X. Zhao, Y. S. Zhang, *Sci. Adv.* **2022**, *8*, eabq6900.
- [22] a) J. Lee, V. Manoharan, L. Cheung, S. Lee, B.-H. Cha, P. Newman, R. Farzad, S. Mehrotra, K. Zhang, F. Khan, M. Ghaderi, Y.-D. Lin, S. Aftab, P. Mostafalu, M. Miscuglio, J. Li, B. B. Mandal, M. A. Hussain, K.-T. Wan, X. S. Tang, A. Khadernhosseini, S. R. Shin, *ACS Nano* **2019**, *13*, 12525; b) W. Zhang, X.-X. Fang, Q.-C. Li, W. Pi, N. Han, *Neural Regen. Res.* **2023**, *18*, 200; c) J.-J. Lee, H. Y. Ng, Y.-H. Lin, E.-W. Liu, T.-J. Lin, H.-T. Chiu, X.-R. Ho, H.-A. Yang, M.-Y. Shie, *Biomater. Adv.* **2022**, *142*, 213132.
- [23] a) Y. Wang, Q. Wang, S. Luo, Z. Chen, X. Zheng, R. K. Kankala, A. Chen, S. Wang, *Regenerative Biomaterials* **2021**, *8*, rbab035; b) E. Cheah, M. Bansal, L. Nguyen, A. Chalard, J. Malmström, S. J. O'carroll, B. Connor, Z. Wu, D. Svirskis, *Acta Biomater.* **2023**, *158*, 87.
- [24] P. C. Sherrell, B. C. Thompson, J. K. Wassei, A. A. Gelmi, M. J. Higgins, R. B. Kaner, G. G. Wallace, *Adv. Funct. Mater.* **2014**, *24*, 769.
- [25] Y. Zhao, S. Zhang, T. Yu, Y. Zhang, G. Ye, H. Cui, C. He, W. Jiang, Y. Zhai, C. Lu, X. Gu, N. Liu, *Nat. Commun.* **2021**, *12*, 4880.
- [26] a) I. M. Taylor, E. M. Robbins, K. A. Catt, P. A. Cody, C. L. Happe, X. T. Cui, *Biosens. Bioelectron.* **2017**, *89*, 400; b) M.-H. Wang, B.-W. Ji, X.-W. Gu, H.-C. Tian, X.-Y. Kang, B. Yang, X.-L. Wang, X. Chen, C.-Y. Li, J.-Q. Liu, *Biosens. Bioelectron.* **2018**, *99*, 99; c) D. Li, M. Liu, Y. Zhan, Q. Su, Y. Zhang, D. Zhang, *Microchim. Acta* **2020**, *187*, 94.
- [27] a) G. Yao, L. Kang, C. Li, S. Chen, Q. Wang, J. Yang, Y. Long, J. Li, K. Zhao, W. Xu, W. Cai, Y. Lin, X. Wang, *Proc. Natl. Acad. Sci. USA* **2021**, *118*, e2100772118; b) Z. Qiao, M. Lian, X. Liu, X. Zhang, Y. Han, B. Ni, R. Xu, B. Yu, Q. Xu, K. Dai, *ACS Appl. Mater. Interfaces* **2022**, *14*, 31655.
- [28] H. Dechiraju, M. Jia, L. Luo, M. Rolandi, *Adv. Sustainable Syst.* **2022**, *6*, 2100173.
- [29] T. Nakajima, H. Sato, Y. Zhao, S. Kawahara, T. Kurokawa, K. Sugahara, J. P. Gong, *Adv. Funct. Mater.* **2012**, *22*, 4426.
- [30] S. De, C. Cramer, M. Schönhoff, *Macromolecules* **2011**, *44*, 8936.
- [31] H. Nara, D. Mukoyama, T. Yokoshima, T. Momma, T. Osaka, *J. Electrochem. Soc.* **2015**, *163*, A434.
- [32] J. L. Gornall, E. M. Terentjev, *Soft Matter* **2008**, *4*, 544.
- [33] L. A. Macqueen, C. G. Alver, C. O. Chantre, S. Ahn, L. Cera, G. M. Gonzalez, B. B. O'connor, D. J. Drennan, M. M. Peters, S. E. Motta, J. F. Zimmerman, K. K. Parker, *NPJ Sci. Food* **2019**, *3*, 20.
- [34] G. Yang, Z. Xiao, X. Ren, H. Long, H. Qian, K. Ma, Y. Guo, *PeerJ* **2016**, *4*, e2497.
- [35] M. K. Mcdermott, T. Chen, C. M. Williams, K. M. Markley, G. F. Payne, *Biomacromolecules* **2004**, *5*, 1270.
- [36] a) S. A. Munim, Z. A. Raza, *J. Por. Mater.* **2019**, *26*, 881; b) M. Grosjean, E. Girard, A. Bethry, G. Chagnon, X. Garric, B. Nottelet, *Biomacromolecules* **2022**. <https://doi.org/10.1021/acs.biomac.2c01166>.
- [37] a) Z. Wu, N. Bouklas, R. Huang, *Int. J. Solids Struct.* **2013**, *50*, 578; b) X. Xue, S. Wang, C. Zeng, L. Li, C. Li, *Surf. Interface Anal.* **2018**, *50*, 180; c) D. Breid, V. Lai, A. T. Flowers, X. Guan, Q. Liu, S. S. Velankar, *Langmuir* **2021**, *37*, 6985.
- [38] W.-C. Huang, X. C. Ong, I. S. Kwon, C. Gopinath, L. E. Fisher, H. Wu, G. K. Fedder, R. A. Gaunt, C. J. Bettinger, *Adv. Funct. Mater.* **2018**, *28*, 1801059.
- [39] X. Zheng, K. M. Woeppel, A. Y. Griffith, E. Chang, M. J. Looker, L. E. Fisher, B. J. Clapsaddle, X. T. Cui, *Adv. Healthcare Mater.* **2019**, *8*, 1801311.
- [40] F. Fallegger, G. Schiavone, E. Pirondini, F. B. Wagner, N. Vachicouras, L. Serex, G. Zegarek, A. May, P. Constantin, M. Palma, M. Khoshnevis, D. Van Roost, B. Yvert, G. Courtine, K. Schaller, J. Bloch, S. P. Lacour, *Adv. Sci.* **2021**, *8*, 2003761.
- [41] a) A. N. Mistry, B. Kachenchart, A. Wongthanaroj, A. Somwangthanaroj, E. Luepromchai, *Polym. Degrad. Stab.* **2022**, *202*, 110051; b) S. S. Soni, A. M. D'Elia, A. Alsasa, S. Cho, T. Tylek, E. M. O'Brien, R. Whitaker, K. L. Spiller, C. B. Rodell, *Biomater. Sci.* **2022**, *10*, 6951; c) S. Wang, J. Li, Y. Pan, F. Liu, L. Zeng, Y. Gao, T. Lu, *Soft Matter* **2022**, *18*, 6192.
- [42] A. Otomo, M. T. Ueda, T. Fujie, A. Hasebe, Y. Suematsu, Y. Okamura, S. Takeoka, S. Hadano, S. Nakagawa, *Sci. Rep.* **2020**, *10*, 6716.
- [43] T. Bréjot, S. Blanchard, M. Hocquemiller, G. Haase, S. Liu, A. Nosjean, J. M. Heard, D. Bohl, *Experimen. Neuro.* **2006**, *198*, 167.
- [44] O. G. Martinsen, S. Grimnes, *Bioimpedance and Bioelectricity Basics*, Academic press, **2011**.
- [45] a) J. Du, J. Liu, S. Yao, H. Mao, J. Peng, X. Sun, Z. Cao, Y. Yang, B. Xiao, Y. Wang, P. Tang, X. Wang, *Acta Biomater.* **2017**, *55*, 296; b) S. Geuna, P. Tos, B. Battiston, *Essays on Peripheral Nerve Repair and Regeneration*, Academic Press, **2009**.
- [46] M. S. Hoseinian, D. Poormoghadam, F. Kheirollahzadeh, A. Mojtahedi, A. Salimi, R. Halabian, *Cur. Stem Cell Res. Ther.* **2022**, *18*, 993.
- [47] J. Wang, P. Jiang, W. Deng, Y. Sun, Y. Liu, *Theranostics* **2022**, *12*, 4288.
- [48] C. M. Madl, B. L. Lesavage, R. E. Dewi, K. J. Lampe, S. C. Heilshorn, *Adv. Sci.* **2019**, *6*, 1801716.
- [49] a) I. Perkućin, K. S. K. Lau, T. Chen, S. N. Iwasa, H. E. Naguib, C. M. Morshead, *Adv. Healthcare Mater.* **2022**, *11*, 2201164; b) I. Cuenca-Ortolá, B. Martínez-Rojas, V. Moreno-Manzano, M. García Castelló, M. Monleón Pradas, C. Martínez-Ramos, J. Más Estellés, *Biomedicines* **2022**, *10*, 2736; c) S. Song, K. W. McConnell, D. Amores, A. Levinson, H. Vogel, M. Quarta, T. A. Rando, P. M. George, *Biomaterials* **2021**, *275*, 120982; d) B.-Q. Lai, R.-J. Wu, W.-T. Han, Y.-R. Bai, J.-L. Liu, H.-Y. Yu, S.-B. Yang, L.-J. Wang, J.-L. Ren, Y. Ding, G. Li, X. Zeng, Y.-H. Ma, Q. Quan, L.-Y. Xing, B. Jiang, Y.-Q. Wang, L. Zhang, Z.-H. Chen, H.-B. Zhang, Y.-F. Chen, Q.-J. Zheng, Y.-S. Zeng, *Biomaterials* **2023**, *297*, 122103; e) R. Guo, M. Xiao, W. Zhao, S. Zhou, Y. Hu, M. Liao, S. Wang, X. Yang, R. Chai, M. Tang, *Acta Biomater.* **2022**, *139*, 105; f) R. D. Bierman-Duquette, G. Safarians, J. Huang, B. Rajput, J. Y. Chen, Z. Z. Wang, S. K. Seidlits, *Adv. Healthcare Mater.* **2022**, *11*, 2101577; g) Z. Guo, C. Sun, H. Yang, H. Gao, N. Liang, J. Wang, S. Hu, N. Ren, J. Pang, J. Wang, N. Meng, L. Han, H. Liu, *Adv. Sci.* **2022**, *9*, 2104424.
- [50] a) A. D. Gaudet, P. G. Popovich, M. S. Ramer, *J. Neuroinflamm.* **2011**, *8*, 110; b) S. Ghosh, S. Haldar, S. Gupta, A. Bisht, S. Chauhan, V. Kumar, P. Roy, D. Lahiri, *ACS Appl. Bio Mater.* **2020**, *3*, 5796; c) J. Lin, J. Shi, X. Min, S. Chen, Y. Zhao, Y. Zhang, L. Cheng, *Front. Bioengineer. Biotech.* **2022**, *9*, 1418.
- [51] M. Zhu, Y. Wang, G. Ferracci, J. Zheng, N.-J. Cho, B. H. Lee, *Sci. Rep.* **2019**, *9*, 1.
- [52] B. H. Lee, H. Shirahama, N.-J. Cho, L. P. Tan, *RSC Adv.* **2015**, *5*, 106094.
- [53] D. N. Rockwood, R. C. Preda, T. Yücel, X. Wang, M. L. Lovett, D. L. Kaplan, *Nat. Protoc.* **2011**, *6*, 1612.

- [54] a) K. Han, Q. Bai, Q. Zeng, N. Sun, C. Zheng, W. Wu, Y. Zhang, T. Lu, *Mater. Des.* **2022**, 217, 110598; b) Y. Yang, K. Shi, K. Yu, F. Xing, H. Lai, Y. Zhou, P. Xiao, *Adv. Healthcare Mater.* **2022**, 11, 2101504.
- [55] J. Penney, W. T. Ralvenius, L.-H. Tsai, *Mol. Psychiatry* **2020**, 25, 148.
- [56] R.-S. Hsu, P.-Y. Chen, J.-H. Fang, Y.-Y. Chen, C.-W. Chang, Y.-J. Lu, S.-H. Hu, *Adv. Sci.* **2019**, 6, 1900520.